UNIVERSITÀ DEGLI STUDI DI PADOVA

Dipartimento di Fisica e Astronomia "Galileo Galilei"

Master Degree in Physics

Curriculum: Physics of Matter

Final Dissertation

Modelling of ion heating by Alfvén waves during magnetic reconnection phenomena in RFP configuration

Thesis supervisor:
Dr. Fabio Sattin
Thesis co-supervisor:
Dr. Marco Veranda

Student:
Alessio Fabbian

Academic Year 2023/2024

Abstract

This thesis deals with the ion-heating by low-frequency electromagnetic (e.m.) waves produced in a magnetic reconnection event. During magnetic reconnection events a fraction of the magnetic energy is converted in kinetic energy of the particles. Despite the study of several heating mechanisms that can contribute to the particle energization, the full mixture of mechanisms operating are still an argument of debate. The ion heating by low-frequency waves is one of the most interesting mechanisms because it could be applied to many types of plasmas, from astronomical to laboratory ones.

In this thesis, we present a modelling of ion heating due to the interaction with a spectrum of Alfvén waves. The Alfvén waves are the lowest frequency e.m. waves that can propagate inside a magnetized plasma. In this thesis, these waves are computed as produced at magnetic reconnection event simulated in 3D nonlinear MHD code. This heating model is based on the hamiltonian formulation of the dynamics of the test-particle.

The ion heating will be studied in several different cases, varying the characteristics of the Alfvén waves, such as the amplitude and the frequency. The duration of the interaction and the mass of the test-particle will be also an argument of discussion.
The most interesting result is connected to the heating given by a broadband spectrum of the magnetic modes excited during a reconnection event in a RFP plasma. The work in this thesis is promising in showing a possible contribution of Alfvén waves to ion heating, comparable with the experimental results.

Contents

Introduction

This thesis summarizes the activities I have carried out and the results I have accomplished during the 6 months collaboration with the Consorzio RFX, at the CNR research area in Padua. Consorzio RFX is a laboratory where science and plasma technology is studied, in particular the focus is on thermonuclear controlled fusion. It hosts two important experiments: the first one is called NBTF (Nuclear Beam Test Facility) and the second one in RFX-mod (Reverse Field eXperiment). NBTF studies the neutral beam injector for the ITER experiment, which is the major international project of a thermonuclear fusion reactor presently under construction in France. RFX-mod is a fusion experiment that studies the reverse-field-pinch (RFP) and Tokamak configurations. It is the largest RFP experiment in the world.

The main topic of this thesis is the ion heating by low-frequency electromagnetic waves produced during a magnetic reconnection event. Ion heating and magnetic reconnection are fundamental topics in plasma physics. They have been experimentally observed and studied in many experimental devices, including the RFP ones.
The magnetic reconnection events change the magnetic topology of the magnetic field lines, and are a topic of intense study: they are related to the action of plasma instabilities and the main signature of a reconnection event is the release of magnetic energy that gets converted into kinetic one. But the mechanism through which this energy is transferred to the particles is still unknown. In years of study, many heating mechanisms were proposed, but none could elaborate a satisfying answer to the problem.

One of the most studied heating mechanism is the ion heating by low-frequency waves. During a reconnection event a large spectrum of electromagnetic turbulence, including Alfvén waves, is generated. They are the e.m. waves with the lowest frequency that can propagate inside a magnetized plasma. So, a heating mechanism that involves the presence of low-frequency waves is a promising solution.

In this thesis, a 3D generalization of the ion-heating model of [1] is presented and discussed. This thesis studies the ion energization given by a spectrum of Alfvén waves obtained at a magnetic reconnection event simulated in a 3D non-linear MHD modelling. This model describes the plasma as a single fluid in an electromagnetic field, and represents one of the most suited models used to study magnetic reconnection in plasma physics. The heating is studied with a test-particle approach, simulating the wave-particle interaction by integrating the equations of motion of the Hamiltonian formulation. The goal of the thesis is assess if particles can be heated by the Alfvén waves produced during a reconnection event.

This thesis develops in 4 main chapters.
The first chapter introduces the concept of thermonuclear controlled fusion. At first, it will be explained why the thermonuclear fusion is so important in the modern world and how we can reach it. With this, it will also be discussed the magnetic confinement, which is the most critical

issue of a fusion reactor.
At the end, there is a recap of the fusion devices, with a more detailed description of the reverse-field-pinch configuration, which is the most important one for the understanding of this thesis.

In the second chapter, the modelling of ion heating is presented and discussed in details after a short recap on resonance systems. The simulation code (the one that computes the equations of motion of the particle) will also be described.

The third chapter is divided in three parts. In the first part, a detailed description of the magnetohydrodynamic model (MHD) of a plasma is given. The main aspects of plasma instabilities and magnetic reconnection phenomena will also be presented. In the second part, the SpeCyl code is introduced: it is a code that numerically solves the equations of the MHD model. This code allows the modelling of a cylindrical plasma in RFP configuration. The last part consists of the description of the analysis performed on the SpeCyl data in order to obtain the spectrum of the Alfvén waves produced in a magnetic reconnection event.

The fourth chapter summarizes all the results of the thesis. In the first part there is a presentation of the Alfvén waves parameters, obtained through the SpeCyl post-processing. There is also a description of how these parameters become an input file for the simulation code.
In the second part, the results of hundreds of independent simulations are presented. They will be divided in two main groups, the simulations with a single low-frequency wave and the ones with a large spectrum of waves. The ion-heating will be analyzed by varying many simulation parameters, such as the simulation time, the mass of the test-particle and the amplitude of the waves. The results in terms of particle energization are promising and comparable with the experimental results.
In the last part, an heuristic interpretation of the ion heating is presented.

Chapter 1

Thermonuclear controlled fusion

In this chapter, a short recap of the basis of thermonuclear controlled fusion is presented.
In the first part, the most relevant nuclear fusions for thermonuclear reactors will be presented. The problem of plasma confinement will be also discussed.
In the last part, we will focus on the fusion devices, in particular the main features of the reverse-field-pinch configuration will be presented. This allows us to move to the RFX-mod machine, which is an RFP device present in Padua, at Consorzio RFX. During the thesis, the characteristic parameters of the RFX-mod machine will be used as reference values.

1.1 The fusion reaction

The study of the thermonuclear controlled fusion is fundamental in a world in which there is an always higher request of energy, because it has the potential to offer an inherently safe and inexhaustible source of energy.
The nuclear fusion is the process in which two light nuclei fuse together generating a new heavier nucleus with the emission of energy in form of kinetic energy of the products. This is the process that guarantees the heat production in the stars.
The easiest fusion reaction, which is the one that happens in stars with a mass lower (or equal) to the Sun, is called pp-chain: it converts 4 protons into a helium atom, emitting 26,73 MeV of energy for every cycle [2]. In the pp-chain (figure 1.1.1) the proton to neutron conversion (step 1) and the He^3 to He^4 conversion (step 3) are governed respectively from weak and strong interactions. These types of interactions are characterized by a very small probability of happening, the first one has a lifetime of $\tau_w \approx 10^9$yr and the second one $\tau_s \approx 10^5$yr. The cross-section of the reaction is the parameter that is used to define the reaction probability: low cross-section means low probability.
The reason why the stars emit a huge amount of energy is that the low probability is compensated by the enormous amount of particles (which are present in the star itself) that can interact for unlimited time in thermal fusion conditions.

On the Earth, it is impossible use the pp-chain for controlled fusion because we cannot maintain the fusion plasma for the time needed to have a significant number of fusion events. It is necessary to find another type of fusion reaction that has an higher cross-section than the pp-chain one. Another important factor which must be consider is that the reactants must be plentiful in nature and easy to obtain.
There are many reactions that satisfy these requirements, but 4 are the simplest ones. All of them require the presence of the deuterium D, which is an isotope of the hydrogen and it is very

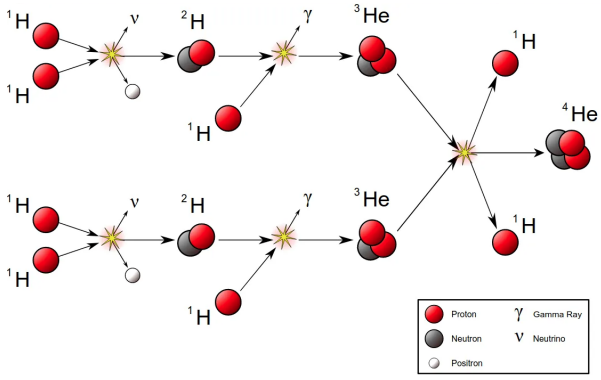

Figure 1.1.1: Representation of the pp-chain of a star. It can be divided in 3 steps: protons to hydrogen conversion, hydrogen to helium-3 and helium-3 to helium-4.

common in nature. The 4 reactions are the following [3]:

$$\begin{aligned} &1) D + D \rightarrow He^3 + n + 3.27MeV \\ &2) D + D \rightarrow T + H + 4.03MeV \\ &3) D + T \rightarrow He^4 + n + 17.6MeV \\ &4) D + He^3 \rightarrow He^4 + H + 18.3MeV \end{aligned} \tag{1.1.1}$$

Studying the cross-sections of these reaction, figure 1.1.2, it is possible to notice that the third one, the reaction between D and T, has the higher cross-section for a large spectrum of operational temperatures. So, the D-T reaction has been selected as the most promising in order to obtain thermonuclear controlled fusion.

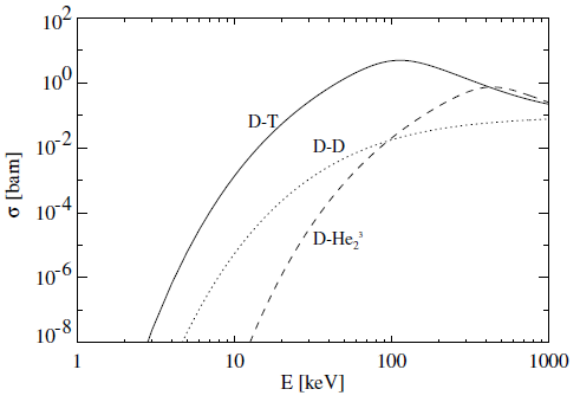

Figure 1.1.2: Cross section [1 barn = $10^{-28}m^2$] of the reactions (eq. 1.1.1) as a function of the kinetic energy [keV] of the Deuterium [3].

This fusion reaction needs the presence of tritium T, which is another isotope of hydrogen. It does not occur in nature because it is a radioactive gas with an half-life of 12 years, but it can be produced quite easily using neutrons to fertilize lithium.

$$\begin{aligned} &Li^6 + n \rightarrow T + He^4 + 4.8MeV \\ &Li^7 + n \rightarrow T + He^4 + n - 2.5MeV \end{aligned} \tag{1.1.2}$$

Due to the fact that the D-T reaction releases a neutron, it is possible to create a chain of events: the D-T fusion reactions produce neutrons that we can make to interact with lithium,

this interaction produces tritium that can be collected and used for other fusion reactions. So, the primary fuel of the fusion reactor are deuterium and lithium, which are very common elements in nature: deuterium can be find in the water (more or less one D atom every 7000 water molecules) and lithium on earth (there are at least 16 millions of tons of Li).

In principle, the simplest approach to obtain fusion is to collide head-to-head two high energy beams, in this case composed by D and T. But this method is not practical due to the fact that elastic collision cross-section is one order of magnitude higher than the fusion one. Since ions undergoing elastic collisions are lost from the beam, it is impossible to have a positive energy balance. So, it is needed a way to confine the plasma in a limited region for a time much larger than the typical elastic collision-time in order to obtain a relevant number of fusion events.

1.2 Plasma confinement

The critical issue of a fusion reactor is the confinement of the plasma.
Plasma is an unstable state of matter. In order to confine it, an external force is needed. For example, a star is a gravitationally-bound sphere of plasma inside which fusion occurs.
In a fusion reactor, the gravity cannot be used for the confinement because the quantity of gas inside the chamber is very low. There are two alternative ways to confine the plasma: the magnetic confinement and the inertial confinement. The first is based on the fact that magnetic forces can confine charged particles along the perpendicular direction to the field, the second, instead, induces fusion bombarding a solid target with high power laser beams. This makes the compression of the inner part and allows to reach the fusion condition.
The magnetic confinement is the one adopted by the European Fusion Program.

When a particle with charge q and velocity $\vec{v}$ is put inside an electromagnetic field it experiences a force, called Lorentz force, which is given by the following equation:

$$\vec{F} = q(\vec{E} + \vec{v} \times \vec{B}) \tag{1.2.1}$$

Neglecting for the moment the electric field $\vec{E}$, this force makes the particle rotate around the direction of the magnetic field $\vec{B}$. If the particle also has a component of the velocity parallel to the $\vec{B}$ field, the resultant trajectory will be a spiral along the field direction. This fact can be used to confine particles, but it works only in the orthogonal plane respect to $\vec{B}$. The Larmor radius r_L and the cyclotron frequency ω_c are two fundamental quantities that describe this type of motion: the first represents the radius of the circular orbit traveled by the particle and the second the angular velocity:

$$r_L = \frac{mv_\perp}{qB} \qquad\qquad \omega_c = \frac{qB}{m} \tag{1.2.2}$$

In order to confine also in the longitudinal direction, the best solution is to close the magnetic field lines on themselves creating a torus. The simplest configuration is the toroidal solenoid: a solenoid is close itself in a doughnut-shaped structure and the magnetic field is only directed along the toroidal direction, which circles around the rotation axis (figure 1.2.1). The poloidal direction, instead, circles around the minor radius of the torus.

The problem of this type of configuration is that the magnetic field inside the torus decreases with the major radius: this can be easily demonstrated by applying the Ampere's law as shown in [3]. The final profile of the magnetic field is the following:

$$B_z = \frac{\mu_0 NI}{2\pi r} \tag{1.2.3}$$

where N is the number of current loops along the toroidal direction and I the current.
This gradient of magnetic field leads the rapid loss of the plasma. The only way to overcome this problem is to superimpose to the original magnetic field, which is called toroidal field, a poloidal component by using external supplies. In this way, the particles experience a helical magnetic field and all the effects of the drift velocity are cancelled by average due to opposite contributions as the particles move around the torus (figure 1.2.1).

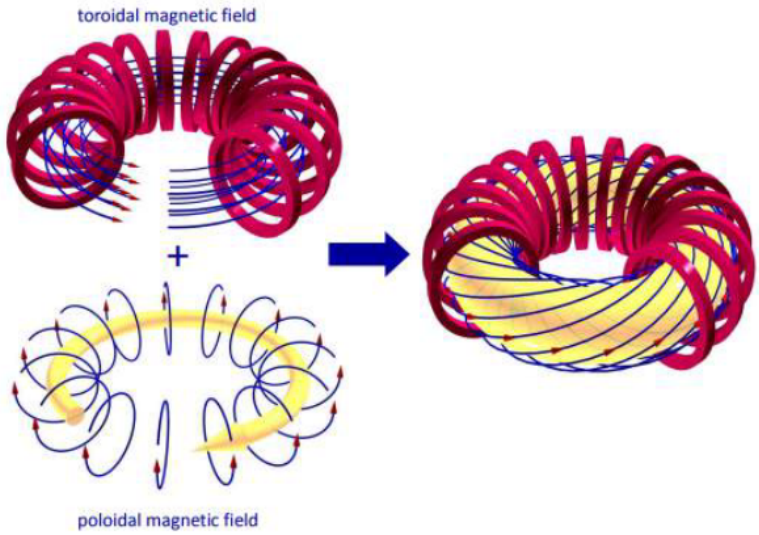

Figure 1.2.1: Representation of the superimposition of the toroidal magnetic field and the poloidal one. The final result is a helical magnetic field that solves the problems of plasma loss due to magnetic gradient.

1.3 Fusion devices

There are 3 main types of toroidal fusion configurations: the Tokamak, the Stellarator and the Reverse Field Pinch (RFP).

The Tokamak is the most developed concept. It features a strong toroidal magnetic field produced by a set of toroidal field coils which approximate a toroidal solenoid (figure 1.3.1). In the central hole, there is the primary circuit, which is nothing but a solenoid which is used to vary the magnetic flux in the central hole. Due to the Faraday's law, this variation induces an electrical current which flows inside the plasma in the toroidal direction. This current, so-called toroidal plasma current, is needed to generate the poloidal magnetic field component which is essential to confine the plasma. The poloidal field is also provided by a set of poloidal coils. Usually, the poloidal component of the field is one order of magnitude smaller than the other one.
The Tokamak is the most promising fusion device because it allows to obtain a stable plasma and it can maintain high temperatures for sufficient long time.

The main difference between the Stellarator and the Tokamak is that the first one has a more complex geometrical structure: it has no more the toroidal symmetry. In fact, the Stellarator is composed by a toroidal tube on which magnetic coils are enveloped along the toroidal direction (figure 1.3.1). This structure generates a complex 3D magnetic field that is very different from the Tokamak one. The advantage of this complex structure is that the magnetic confinement

is reached without using a toroidal current: it is a current-less device. The complexity of the design makes them more difficult to project, but this is compensated by the great stability of the plasma: the presence of a toroidal current is the principal reason of plasma instabilities.
The RFP has some similarities to the Tokamak structure, and it will be discuss in details in the next section.

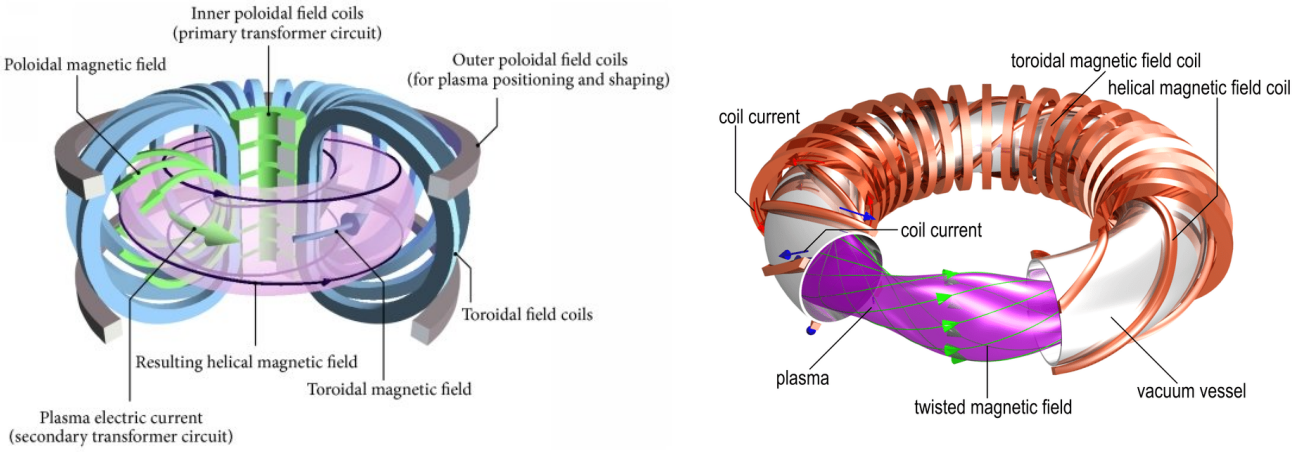

Figure 1.3.1: Scheme of a Tokamak device (left) and a Stellarator (right).

1.3.1 The reversed-field-pinch

The reverse-field-pinch (RFP) is the third most developed fusion device. The research in the case of RFP is not yet developed at the level of the largest tokamaks or stellarators due to the better results obtained by the last two configurations in terms of plasma temperature.
The RFP is a toroidal pinch device that can be obtained from the Tokamak one with some adaptation of the power supplies. In the same way, RFP devices can be used in tokamak configuration. In fact, they have in common the same axisymmetric chamber, but in the RFP the toroidal plasma current is one order of magnitude higher than the Tokamak's one using the same magnetic flux.

Due to the high level of the current, the poloidal magnetic field has the same magnitude of the toroidal one. This is one of the main differences with the Tokamak devices. In figure 1.3.2, it is possibile to see the comparison of the radial profile of the toroidal B_ϕ and poloidal B_θ magnetic field of Tokamak and RFP. It is possible to notice that the B_ϕ component of the RFP changes sign near the edge of the chamber. This is the reason of the name "reversed field".
This inversion can be measured through the reversal parameter F, which is the ratio between B_ϕ at the edge (a is the plasma minor radius) and the volume averaged value. The parameter Θ is the so-called pinch parameter, which differs from F for the presence of the B_θ. These two parameters are externally measurable and they are used to characterize the RFP operations and allow to compare results of different experiments.

$$F = \frac{B_\phi(a)}{< B_\phi >} \qquad \Theta = \frac{B_\theta(a)}{< B_\phi >} \tag{1.3.1}$$

The features of RFP give some potential technological advantages respect to the tokamak configuration. First of all, the external coils have to produce only a small part of the magnetic field because the bigger part is produced by the current which is flowing in the plasma. This means that the structure of the external coils can be simpler: for example in a RFP superconductive

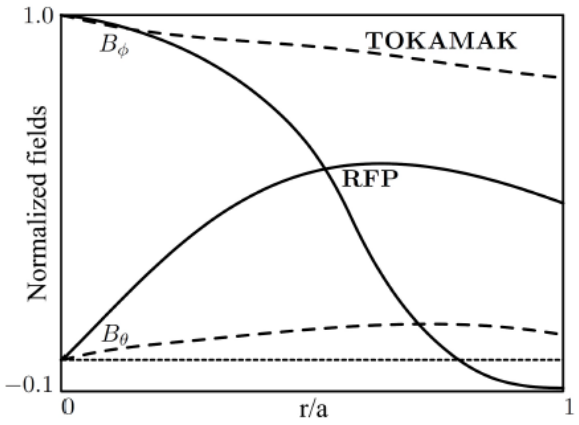

Figure 1.3.2: Comparison of the radial profile of the magnetic field components B_θ and B_ϕ of Tokamak and RFP devices. It is possible to see the characteristic field inversion near the edge for the RFP plasma.

materials are not required such as the related cooling systems.
Another advantage is that a RFP plasma could be heated up at higher temperatures using the ohmnic heating, due to the fact that in it flows a very high current. So, it is possible to not consider other types of heating, as radio-frequency and neutral beam injection.
On the other hand, RFP is characterized a mixture of magnetic modes (Chapter 3) that make the magnetic field chaotic. This gives problems in terms of plasma confinement and heating.

1.3.2 The RFX-mod device

The RFX-mod device is the largest RFP experiment in the world and it is located in Padua, Italy, at Consorzio RFX.

The main parameters that defines the RFX-mod experiment are shown in the table 1.

Major radius	R_0	2.00 m
Minor radius	a	0.459 m
Max plasma current	I	2.0 MA
Max magnetic field	B	0.7 T
Vacuum pressure	P_v	10^{-10} Pa
Plasma pressure	P_p	10^3 Pa
Plasma density	n_p	$5 \cdot 10^{19} m^{-3}$
Max electron temperature	T_e	1.5 KeV
Max duration discharge	t	0.5 s

Table 1.1: Main parameters that define the RFX-mod device.

The toroidal device is composed by the toroidal vacuum vessel, magnetic systems for producing plasma equilibrium and control, power supplies and diagnostics that surround the machine. The machine is shown in figure 1.3.3 during its operational phase.
The internal wall, that directly faces the plasma, is composed by 2016 graphite tiles. This composition was chosen in order to sustain the thermal loads and to get a low-impurities flow inside the plasma.
The vacuum vessel that allows reaching low pressures is composed by 72 wedge shaped elements

that are sustained by the external mechanical structure. The magnetic system is composed by 3 windings: the toroidal field coils (48 coils) for the production of the toroidal magnetic field B_ϕ, the poloidal field coils (20 coils) for the B_θ production and the vertical coils (16), described in [4]. The main aim of this system is to control the shape and position of the plasma.
The RFX-mod experiment also has a system of 192 saddle coils dedicated to plasma active control. Today, the RFX-mod device is facing a shut down to allow the upgrading of the device to its second version, called RFX-mod2. The figure 1.3.4 shows a typical signal obtained during a

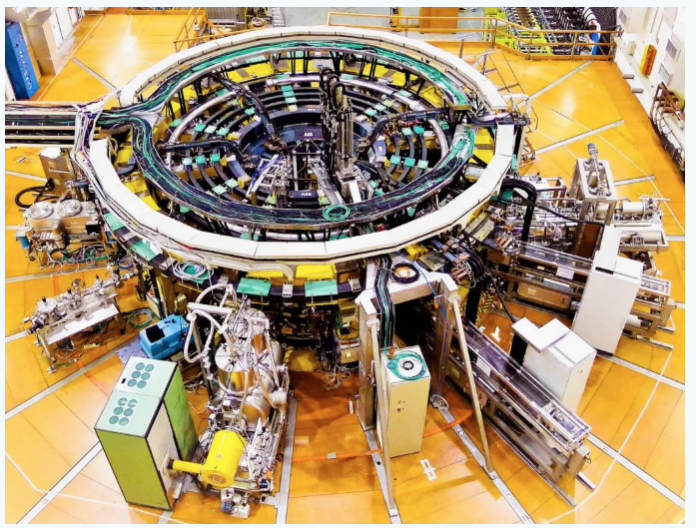

Figure 1.3.3: The RFX-mod device.

RFX-mod discharge. On the first row the reversal and pinch parameters, F and Θ, are shown. On the second row the behaviour of the toroidal component of the magnetic field at the edge, for the most significant MHD modes (that will be described in the chapter 3), is presented. The third row shows the temporal behaviour of the electron temperature on the torus' axis. The maximum temperature reached in this kind of discharges is around 800 eV and the typical density is $n = 2 \cdot 10^{19} m^{-3}$ for $I_p = 1.2MA$.

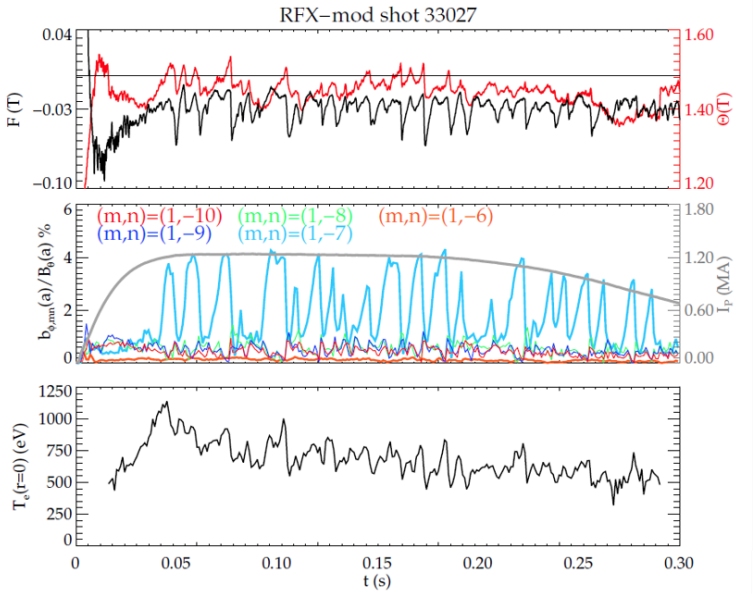

Figure 1.3.4: Experimental data of the RFX-mod machine.

Chapter 2

Modelling of ion heating

In this chapter, the modelling of ion heating is presented. It is a test-particle approach, in which the dynamics of a particle, that interacts with a prescribed low-frequency wave, is studied by the Hamiltonian description. Before its introduction, a recap of the concept of resonance is presented. In the second part, a comparison of the normalizations used in this thesis is discussed. In the last part, a general introduction to the simulation code is given. This will be useful for the right interpretation of the final results.

2.1 Resonance of a system

The resonance is a physical phenomenon that can be studied in many sectors of physics, from mechanics to electromagnetism. It becomes important everytime we are dealing with oscillatory dynamical systems. In general, we have resonance when an external force F_{ext} acts on a oscillating system amplifying its amplitude in the time.
This happens only if the F_{ext} is applied to the system with a precise frequency, the so-called resonance frequency. Often, systems possess a resonant frequency, which depends on their physical characteristics such as the dimension and the mass: it is also called natural frequency.

The simplest case in which we can study the resonance is the harmonic oscillator:

$$m\frac{d^2x}{dt^2} = -\omega_0^2 x \tag{2.1.1}$$

Its natural frequency is given by ω_0. This frequency does not depend on the amplitude of the motion: it means that even if the kinetic energy of the mass increases, so the amplitude of the motion increases too, the frequency of the oscillation does not change.

If we apply to the system an external force proportional to this frequency, for example $F_{ext} \propto cos(\omega_o t)$, this force will be in phase with the oscillator: it means that the oscillator, in its reference frame, will see the external force as constant. A constant force applied to the system corresponds to a constant acceleration that will increase the kinetic energy, so the amplitude of the oscillations. Applying the generical $F_{ext} = f_0 cos(\Omega t)$, the equation 2.1.1 become [5]:

$$m\frac{d^2x}{dt^2} + \omega_0^2 x = f_0 cos(\Omega t) \tag{2.1.2}$$

By solving this differential equation for the initial condition $x(0) = 0$ and $\frac{dx}{dt}(0) = 0$ we obtain:

$$x(t) = \frac{f_0}{m(\omega_0^2 - \Omega^2)} sin(\Omega t) \tag{2.1.3}$$

In resonance condition, $\Omega = \omega_0$, the position diverges: it means that the oscillations become always bigger, so the kinetic energy increases.
So the resonance is a physical feature which can be used for the acceleration (or heating) of oscillating objects. Another interesting case, connected to the topic of this thesis, is the acceleration of charged particles inside a toroidal structure. As seen in section 1.2, charged particles can be confined in a toroidal chamber thanks to the imposition of a magnetic field. In that case, the natural frequency is the one of the periodic rotation along the toroidal direction, the cyclotron frequency (eq. 1.2.2). In this case, it is possible to accelerate the particles by introducing in the chamber an electromagnetic wave in phase with the particle motion: the particle will experience a constant electric field that will heat it [6].

We remark the fact that the ion heating described in this thesis is not due to the resonance between particle and wave. In fact, the Alfvén wave's frequency is very lower than the cyclotron frequency of the test-particle (as you will see in section 4.1.1). A possible interpretation of the heating will be given in the last section 4.4.

2.2 Hamiltonian description of the heating modelling

The goal of this thesis is to try to generalize the ion heating modelling proposed in [1] to a more complex 3D system and investigate if it could be a plausible heating mechanism in the case at hand. In [1], a 1D modelling of ion heating is proposed, in which particles are made to interact with a single Alfvén wave for a limited time. This phenomenum is studied by the 1D Hamiltonian description of the wave-particle interaction.
In this thesis the idea is the same, studying the interaction between particles and a spectrum of Alfvénic turbulence, but this time in a 3D magnetic field.
We want to see if the particles can be heated by the low-frequency waves that are produced by a magnetic reconnection event in a reversed-field-pinch plasma. This is done by a non-self-consistent test-particle approach, in which ions are mutually independent particles interacting with a prescribed set of waves.

The logical steps of this type of calculation are basically two. First of all, it is necessary to find and study the Alfvén waves produced in a RFP plasma. It is not possible to have experimental results on the Alfvén waves propagation inside the chamber, the only result is given by [7] in which the presence of Alfvén waves is shown at the edge of the chamber. For this reason, the Alfvén waves used in this thesis are obtained by analyzing simulation data produced by the SpeCyl code. All the details connected to the Specyl code, the 3D magnetic structure of a RFP plasma and the computation of the Alfvèn waves produced by a reconnection event will be explained in the next chapter.
The second step is to make the particles interact with these waves. By using a fortran90 code solving the ion-heating model, this interaction was simulated for a huge number of particles and the average energy gain was computed.

The modelling starts from considering a toroidal device of a RFP plasma, in which an equilibrium magnetic field is present. The word "equilibrium" refers to a static magnetic field, whose components have a spatial dependence on the three toroidal coordinates (r, θ, ϕ), but they do not depend on time. In order to simplify the calculations, we will use cylindrical coordinates (r, θ, z) instead of toroidal ones. In the appendix A.2, there is a short description of how cylindrical coordinates can be used for the toroidal description. The idea is to implement a boundary condition along the z-direction in order to consider the periodicity of the toroidal

shape: this allows to convert the z-axis in a new angular variable ϕ. During this thesis, z and ϕ will be both used for the description of the toroidal direction.

A test-particle, with charge q and mass m, which is put inside the plasma, will start rotating along the toroidal direction with a spiraling trajectory and it will be confined in the radial direction. This will be an adiabatic motion: the total energy of the particle will be conserved through its trajectory. In this thesis, the test-particle will be almost always a hydrogen ion, $q = 1.6 \cdot 10^{-19} C$ and $m_H = 1.67 \cdot 10^{-27} Kg$.
The test-particle motion can be described through its Hamiltonian. It is known from classical mechanics that, in order to construct the Hamiltonian of a particle that interacts with an electromagnetic field, it in necessary to introduce the minimal coupling, which changes the canonical momentum $\vec{p}$ in the quantity $\vec{p} - q\vec{A}$, with A the vector potential of the field [8].
The general structure of the hamiltonian of these types of systems is the following, in which $V(\vec{x})$ is the scalar potential of the field:

$$H(\vec{x}, \vec{p}) = \frac{1}{2m} |\vec{p} - q\vec{A}|^2 + qV(\vec{x}) \tag{2.2.1}$$

In our case, we do not consider electric fields inside the chamber, so we set $V(\vec{x}) = 0$.
In order to implement the magnetic field inside this equation, its vector potential must be computed, as described in section 3.6.3. The vector potential of the equilibrium field will be called $\vec{A}^{0,0}(r, \theta, z) = \vec{A}^{0,0}(r)$ referring to the axisymmetric field of the SpeCyl code, section 3.4.

The particle will start to interact with the perturbation, that will make it oscillate. The particle will be always confined inside the toroidal chamber due to the small magnitude of the perturbation. The vector potential of perturbation field will be called $\vec{A}^{m,n}(r, \theta, z)$, referring to the mode (m,n) of the Fourier decomposition described in section 3.4.1.

The particle will feel a total electromagnetic field which is the superimposition of equilibrium and perturbation ones. The j-th component of the total vector potential ($j = r, \theta, z$) is simply the sum of the two terms:

$$A_j(r, \theta, z, t) = A_j^{0,0}(r) + A_j^{m,n}(r, \theta, z, t) \tag{2.2.2}$$

It was assumed that the Alfvén wave could be described as a plane wave, with an harmonic function of the type $f(\vec{r}, t) = f_{max} e^{i(\vec{k} \cdot \vec{r} - wt)}$, with $\vec{k}$ the wave vector and ω the wave frequency. The simplest shape for a plane wave comes from neglecting the imaginary part. In this way, the wave is described by an amplitude factor f_{max} multiplied to a cosine function $cos(\vec{k} \cdot \vec{r} - \omega t)$.

The perturbation term of the equation 2.2.2 could be re-written in the following shape:

$$A_j^{m,n}(r, \theta, z, t) = A_j^{m,n}(r) \cdot cos(\vec{k} \cdot \vec{r} - \omega t) = A_j^{m,n}(r) \cdot cos(k_r r + m\theta - \frac{nz}{R_0} - \omega t) \tag{2.2.3}$$

The $A_j^{m,n}(r)$ term, which represented the amplitude of the wave, is the radial profile of the j-th component of the vector potential of the mode (m,n). This quantity was obtained directly from the SpeCyl data, as described in the section 3.6.3.

In this system, it is also possible to neglect the collisions with other particles because the typical ion-ion collision time is of the order of $10^{-4} s$, which is very higher than the scale time $\tau_A \approx 10^{-7} s$. This means that the thermalization of the particles induced by the collisions is neglected (so we should talk about particle energization, and not heating, but we will use both terms remembering this assumption).

Once obtained the complete description of the vector potential, it can be substituted inside the hamiltonian, eq. 2.2.1. It is an non-autonomous hamiltonian due to the presence of the peturbation field.
The equations of motion, the Hamilton equations, have been numerically computed in the simulation code by using a symplectic integrator. This type of integrators is typically used for the integration of Hamiltonian dynamical systems because it preserves the Poincarè integral invariants of the Hamiltonian flow, without corrupting the long-time dynamics of the system. More details about symplectic integrators can be find the appendix A.4 and in the papers [9-10].

2.2.1 Normalization of the main quantities

A convenient way to simplify the calculations is to introduce the normalization of all the equations of the system to some reference values.
In this thesis two different codes have been used: the fortran code, that computes the particle motion, and the SpeCyl code, needed for the MHD modelling. These codes have been originally written with different normalizations, so the translation of the SpeCyl data into a correct input file for the simulation code is a delicate step.
For this reason, in this section we will present a detailed description of the two normalizations.

The physical quantities which are present in the SpeCyl code are normalized as follows: from now, a normalized quantity will be described through a tilde on the top of the quantity.

- Time: normalized to the Alfvén time τ_A (eq. 2.2.20);

$$t = \tilde{t}\ \tau_A \tag{2.2.4}$$

  The Alfvén time is computed by the following equation:

$$\tau_A = \frac{a\sqrt{\mu_0 n_i m_H}}{B} \approx (2.07 \cdot 10^{-17}) \frac{n_e^{1/2} \gamma^{1/2}}{z^{1/2} B} [s] \tag{2.2.5}$$

  in which n_e is the electron density, γ is the ratio between the considered test-particle mass and the hydrogen one, z the ratio between the number of electrons and ions in the system and B the magnetic field.
  The SpeCyl simulation used in this thesis considers an hydrogen plasma, whose Alfvén time is $\tau_A \approx 7.8 \cdot 10^{-8}$s;

- Magnetic field: normalized to the max value of the z-component of axisymmetric field $B_z^{0,0}$ computed by the SpeCyl code at r=0 and t=0;

$$B = \tilde{B}\ B_z^{0,0} \tag{2.2.6}$$

- Length: normalized to the minor radius a of the RFX-mod experiment (Table 1);

$$r = \tilde{r}\ a \tag{2.2.7}$$

- Density: normalized to a fixed given density ρ_0.

Given all these quantities, any other one that appears in the equations is automatically normalized. For example, the velocity can be easily normalized through the normalization of time and space:

$$v = \frac{\Delta r}{\Delta t} = \frac{a\Delta\tilde{r}}{\tau_A \Delta\tilde{t}} = \tilde{v}\frac{a}{\tau_A} = \tilde{v}\ v_A \tag{2.2.8}$$

By definition, v_A is the Alfvén velocity.

The fortran code equations, instead, have been normalized as follows:

- Mass: normalized to the test-particle mass;

$$m = \tilde{m}\ m_i \tag{2.2.9}$$

- Electric charge: normalized to the test-particle charge;

$$q = \tilde{q}\ e_i \tag{2.2.10}$$

- Time: normalized to the inverse of the cyclotron frequency of the test-particle;

$$t = \tilde{t}\ \omega_i^{-1} \tag{2.2.11}$$

  For simplicity, in all then thesis we will express the time parameters of the code (such as the simulation length) in units of τ_A, because is the typical time scale of the system.

There are two main equations that must be normalized: the first one is the definition of the vector potential and the second one is the Hamiltonian, which returns the energy factor needed for the conversion of the simulation output data.

The first one is quite simple, because it follows by the normalization of the magnetic field. The starting equation is $\nabla \times A = B$ and the normalization steps are the following:

$$\frac{1}{a}\tilde{\nabla} \times A = \tilde{B}B_z^{0,0} \qquad \tilde{\nabla} \times A = \tilde{B}B_z^{0,0}a \rightarrow A = \tilde{A}B_z^{0,0}a \tag{2.2.12}$$

The normalization of the Hamiltonian needs the introduction of another quantity, the momentum, which can be normalized by using the velocity:

$$p = mv = \tilde{m}m_i\tilde{v}v_A = \tilde{m}\tilde{v}\frac{am_i}{\tau_A} \rightarrow p = \tilde{p}\frac{am_i}{\tau_A} \tag{2.2.13}$$

Starting from the equation 2.2.1 the Hamiltonian becomes:

$$H = \frac{1}{2\tilde{m}m_i}|\tilde{p}\frac{am_i}{\tau_A} - \tilde{q}\tilde{A}eB_z^{0,0}a|^2 \tag{2.2.14}$$

Now, it is possible to introduce the cyclotron frequency (eq. 1.2.2) of the particle in the equilibrium field, which is normalized by the inverse of the Alfvén time:

$$\omega_c = \frac{eB_z^{0,0}}{m_i} \rightarrow \omega_c = \frac{\tilde{\omega_c}}{\tau_A} \tag{2.2.15}$$

Introducing this quantity in the potential vector term of the equation 2.2.13, it follows that

$$H = \frac{1}{2\tilde{m}m_i}|\tilde{p}\frac{am_i}{\tau_A} - \tilde{q}\tilde{A}am_i\omega_c|^2 = \frac{1}{2\tilde{m}m_i}|\tilde{p}\frac{am_i}{\tau_A} - \tilde{q}\tilde{A}\tilde{\omega_c}\frac{am_i}{\tau_A}|^2 \tag{2.2.16}$$

Now it is possible to take the $\frac{am_i}{\tau_A}$ term out of the parenthesis, raising it to the 2nd power. The final step gives

$$H = \frac{a^2m_i}{2\tilde{m}\tau_A^2}|\tilde{p} - \tilde{q}\tilde{A}\tilde{\omega_c}|^2 \rightarrow H = \tilde{H}\frac{a^2m_i}{\tau_A^2} \tag{2.2.17}$$

$$\tilde{H} = \frac{1}{2}|\tilde{p} - \tilde{A}|^2 \tag{2.2.18}$$

This is the hamiltonian from which the Hamilton equations are performed by the simulation code. The terms $\tilde{m}, \tilde{q}$ and $\tilde{\omega}_c$ are all equal to 1 due to the normalization.
The term $\frac{a^2 m_i}{\tau_A^2}$ which must be multiplied to the normalized energy corresponds to $390keV$. It interesting to note that this value does not depend on the mass of the particle, in fact eq. 2.2.20 tells that $\tau_A \propto \sqrt{m_i}$. This means that if the test-particle is changed, the energy factor will be the same.
For the normalization of the magnetic field, experimental data coming from the RFX-mod device were observed. It was decided to use a value of $B_z^{0,0} = 1.3T$, which corresponds to the magnetic field of a toroidal plasma with a toroidal current of $I_t = 1.3MA$.

2.2.2 Simulation code

The simulations of the motion of the particle which interacts with the Alfvén wave is performed by a Fortran90 code. This code takes as input two different files:

- The first file contains the radial profile of the vector potential in cylindrical coordinates. How these fields were computed is presented in the section 3.6.3;
- The second file is a list of parameters. They are divided in three groups: the first is for the initial conditions of the particle, the second for the wave parameters and the last one for the time parameters. The list is structured as follows:

  - x_0, y_0, z_0 are the cartesian coordinates of the initial position of the particle;
  - $v_{x_0}, v_{y_0}, v_{z_0}$ the three components of the initial velocity;

  - k_r the maximum amplitude of the radial wave vector (see section 3.6.2);
  - ω_k the periodicity of k_r along the radial direction (see section 3.6.2);
  - ω the frequency of the Alfvén wave;

  - t_{max} is the duration of the simulation;
  - t_f, t_s, dt are the time parameters that define the shape function $f(t)$ (that will be described later in this section);
  - h is the timestep;
  - $nhsave$ defines how much frequently the program has to write data in the txt file.

It was decided to compute the hamiltons' equations of eq. 2.2.18 in cartesian coordinates, because they are simpler to treat in these coordinates. This is the reason of the choice of the initial conditions showed before.
On the other hand, it was necessary to make the code compatible with the input data that were expressed in cylindrical geometry.
The idea was to make this coordinate change runtime by following a list of steps:

- Given $P_t = (x, y, z)$ the position of the particle at time t in cartesian coordinates, the related cylindrical coordinates are performed by the equations $\rho = \sqrt{x^2 + y^2}$ and $\theta = arctg\frac{y}{x}$;
- The generic input quantity Q defined in cylindrical coordinates (such as the vector potential) must be calculated at that spatial position $P_t = (\rho, \theta, z)$. Due to the fact that the quantity Q is usually defined in a radial mesh of 100 steps between $[0, 1]a$, it is necessary to

do an interpolation of the data. It was checked the difference between linear and quadratic interpolation and, after having noticed that there were no significant differences between the two, the linear one was selected. Linear interpolation is performed only on the radial and the θ directions, because the z-one is not influenced by this the change of coordinates.

- The matrix of change of variables from cartesian to cylindrical coordinates is inverted and applied to the Q-vector computed in P_t. The final result is the Q-vector computed in P_t in cartesian coordinates:

$$\begin{bmatrix} Q_r \\ Q_\theta \\ Q_z \end{bmatrix} = \begin{bmatrix} cos\theta & sin\theta & 0 \\ -sin\theta & cos\theta & 0 \\ 0 & 0 & 1 \end{bmatrix} \begin{bmatrix} Q_x \\ Q_y \\ Q_z \end{bmatrix} \rightarrow \begin{bmatrix} Q_x \\ Q_y \\ Q_z \end{bmatrix} = \begin{bmatrix} cos\theta & -sin\theta & 0 \\ sin\theta & cos\theta & 0 \\ 0 & 0 & 1 \end{bmatrix} \begin{bmatrix} Q_r \\ Q_\theta \\ Q_z \end{bmatrix} \tag{2.2.19}$$

$$\begin{cases} Q_x(x,y,z,t) = Q_r(\rho,\theta,z,t)cos\theta - Q_\theta(\rho,\theta,z,t)sin\theta \\ Q_y(x,y,z,t) = Q_r(\rho,\theta,z,t)sin\theta + Q_\theta(\rho,\theta,z,t)cos\theta \\ Q_z(x,y,z,t) = Q_z(\rho,\theta,z,t) \end{cases} \tag{2.2.20}$$

This procedure has been applied to the vector potential, both axisymmetric and perturbation one, and to the radial component of the wave vector.

In order to study a realistic case of wave-particle interaction, the simulation length must be comparable with the duration of the simulated reconnection event. Exploring the temporal evolution of many magnetic modes, it was decided to fix the simulation length to the value of $600\tau_A$, which is an average value observed.
The other time parameters (t_f, t_s, dt) define the structure of the shaping function $f(t)$. This function works as a switch: it starts and stops the perturbation. It has been introduced to have the possibility to observe the behaviour of the system in three different steps, the initial equilibrium, the perturbation phase and the final equilibrium.
It is necessary to set $f(t)$ parameters in order to have a extremely slow switching-on/off with respect to the typical time-scale of the system. A rapid variation of the magnetic field leads to the generation of a electric field due to the Maxwell's law $\vec{\nabla} \times \vec{E} = -\frac{\partial \vec{B}}{\partial t}$. Only with a slow variation of the field it was possible to neglect the electric field contribution to the equation of motion of the particle.
The $f(t)$ shape was the following:

$$f(t) = \frac{1}{4}\left[1 + tanh\left(\frac{t - t_s}{dt}\right)\right]\left[1 + tanh\left(\frac{t_f - t}{dt}\right)\right] \tag{2.2.21}$$

In figure 2.2.1, an example of the temporal evolution of the $f(t)$ function is shown. In order to have an interaction of the order of $600\tau_A$, the time parameters that defined the shape function $f(t)$ must be as $t_{max} = 1000\tau_A$, $t_f = 0.2t_{max} = 200\tau_A$ and $t_s = t_{max}(1 - 0.2) = 800\tau_A$, with a $dt = 0.2t_f = 40\tau_A$.
The simulations that have been performed with different time parameters will be signaled during the thesis.

The $f(t)$ function has been applied to both eq. 2.2.2 and 2.2.3 as shown in the following equation:

$$\vec{A}(r,\theta,z,t) = \vec{A}^{0,0}(r,\theta,z) + \vec{A}^{m,n}(r) \cdot cos(k_r r + m\theta - \frac{nz}{R_0} - \omega t)f(t) \tag{2.2.22}$$

The timestep h of the simulation was checked by performing many simulations varying the h-value between $[10^{-4}, 10^{-2}]\omega_i^{-1}$. No relevant differences were noted varying the timestep in this range. It was decided to set the h-value at $h = 10^{-3}\omega_i^{-1} = 2 \cdot 10^{-2}\tau_A$ as a compromise between computational costs and precision of the calculations.

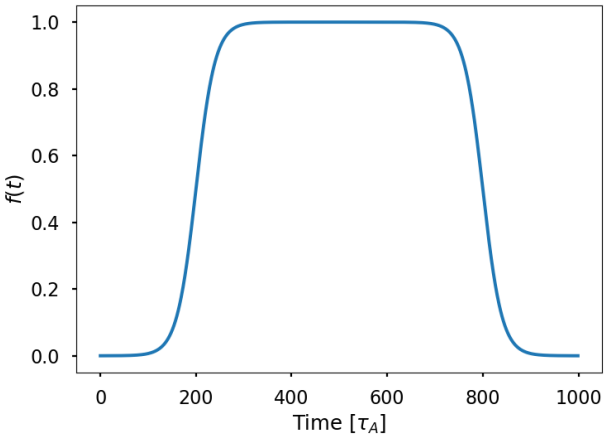

Figure 2.2.1: Example of the temporal profile of the $f(t)$ function for a simulation of $1000\tau_A$. It is possible to see that only in a region about $600\tau_A$ wide the perturbation acts entirely.

Chapter 3

MHD plasma modelling

The plasma is a complex system composed by different types of particles that interact trough electromagnetic forces. There are many models that try to describe different characteristics of the plasma.
In this chapter, a full description of the magnetohydrodynamic model (MHD) is presented. It is fundamental for the description of plasma instabilities and also for the definition of the Alfvén waves, that are considered in this thesis.
In the second part, there is a short description of the SpeCyl code, which numerically integrates the equations of visco-resistive MHD model in cylindrical geometry. This code gave us the instruments for obtain a full description of the Alfvénic turbulence that is generated inside a RFP plasma during a magnetic reconnection event.
The last part shows the analysis performed on SpeCyl data in order to obtain the Alfvén waves parameters. These parameters will be input files of the simulation code described in the previous chapter.

3.1 Dynamical theories for plasmas

A dynamical theory is a physical theory with which the time evolution of a system can be studied. Every dynamical theory, that can be defined in this way, must follow two fundamental characteristics: it must have a way to describe the state of a system at time t by using a set of variables and it must have a set of equations that describe the time evolution of these variables.

When we are talking about fluids and plasmas, there are many different levels of theory that can be applied [11]. It is possible to start from the quantum level, in which the system is considered to be composed by N quantum particles that can be described by using the N-particle wave function, which evolves in time according to the Schroedinger's equation.
If the typical dimension of the system is larger than the de Broglie wavelength $\lambda = \frac{h}{p}$, the wave packets can be considered widely separated, so the quantum interference is negligible. In that case, it is possible to move to next level, the classical mechanics, considering the system composed by N classical particles which follow the Newton's laws of motion.
If the number of particles N is very large, it becomes very hard to solve a system of 6N equations of motion for positions and velocities of the particles. The successive level is the introduction of a particle distribution function to describe the evolution in time of the system. This is the typical level of the statistical mechanics.
From this, it is quite easy to move to the last level, the continuum level, in which the system is not more considered as composed by particles, but as a single element.

In order to study a plasma, it is possible to start from a microscopic approach, defining a particle distribution function $f(x, v, t)$ and studying its time evolution. Applying the corollary

of the Liouville's theorem, which tells that the phase-space volume occupied by N particles cannot change in time [A1], it is possible to obtain the Vlasov's equation:

$$\frac{\partial f(\vec{x},\vec{v},t)}{\partial t} + \vec{v}\cdot\vec{\nabla}_x f(\vec{x},\vec{v},t) + \frac{\vec{F}}{m}\cdot\vec{\nabla}_v f(\vec{x},\vec{v},t) = 0 \tag{3.1.1}$$

It describes the time evolution of a distribution function in a system in which long-distance interactions are included.
Introducing the distribution functions for ions and electrons, this equation leads to the two-fluid model by computing the moment equations. A more detailed description can be find in [12]. In this model the plasma is regarded as an inter-penetrating mixture of a negatively charged fluid of electrons and a positive one composed by ions. Due to the fact that the Vlasov equation cannot handle collisions, the two-fluid model will be appropriated only for non-collisional plasmas. .

If we want to re-introduce collisions in the plasma description, a set of new assumptions must be included. The first one is connected to the length scale: the portion of fluid that is studied must be larger than the Debye's length $\lambda_D = \sqrt{\frac{\epsilon_0 k T_e}{n_e q_e}}$, which represents the distance beyond which the electric field is screened by the motion of the free electric charges. Over the Debye's length, the plasma can be considered quasi-neutral. The second is the non relativistic approximation, which neglects the second order of the Lorentz's transformations of fields. These hypothesis allow to consider the plasma as a single conductive fluid of electrons and ions. Starting from the momenta equations, it is possible to derive the single-fluid model, which is known as magnetohydrodynamics model (MHD). It is one of the most used models for the studying of plasma systems.

The complete set of equations of the MHD model is the following:

$$\begin{aligned}
&Generalized\ Ohm's\ law: \vec{E} + \vec{v}\times\vec{B} = \frac{\vec{J}\times\vec{B} - \nabla p_e}{en} + \eta\vec{J} \\
&Maxwell's\ equations: \vec{\nabla}\cdot\vec{B} = 0 \qquad \vec{\nabla}\times\vec{B} = \mu_0\vec{J} \qquad \vec{\nabla}\times\vec{E} = -\frac{\partial\vec{B}}{\partial t} \\
&Continuity\ equation: \frac{\partial\rho}{\partial t} + \vec{\nabla}\cdot(\rho\vec{v}) = 0 \\
&Equation\ of\ motion: \rho\left[\frac{\partial\vec{v}}{\partial t} + (\vec{v}\cdot\vec{\nabla})\vec{v}\right] = \vec{J}\times\vec{B} - \vec{\nabla}p + \rho\nu\nabla^2\vec{v} \\
&Induction\ equation: \frac{\partial\vec{B}}{\partial t} = \vec{\nabla}\times(\vec{v}\times\vec{B}) + \eta\nabla^2\vec{B}
\end{aligned} \tag{3.1.2}$$

The main quantities of these equations are: electric field E, magnetic field B, current density J, velocity field v, density ρ and pressure p.
There are also two fundamental parameters, the electrical resistivity η and the viscosity ν.
If we compare the MHD model with the hydrodynamic model for neutral fluids, we can notice some important differences. First of all, the presence of the Ohm's law and the Maxwell's equations, due to the electromagnetic properties of the plasma. Another difference is the presence of a magnetic force term inside the equation of motion. In the end, the induction equation is a completely new equation. It is the magnetic version of the vorticity equation of fluids and, for MHD model, it becomes a fundamental equation in order to have a full dynamical theory.

To summarize, a state in MHD model is described by 8 scalar variables: two thermodynamic quantities (ρ, p), 3 components of the velocity field and 3 of the magnetic field.

This is the most general form of the model. Typically, two different versions are used:

- Ideal MHD model: the resistivity η and the viscosity ν of the plasma are considered equal to zero (This allows to neglect the Ohm's law);

- Visco-resistive MHD model: the resistivity η and the viscosity ν must be considered, such as the Ohm's law.

A further simplification of the MHD model is the neglecting of the $\frac{\vec{J}\times\vec{B}-\nabla p_e}{en}$ term in the generalized Ohm's law. This is possible when it is very low if compared with the other terms of the equation. In that case, the generalized Ohm's law becomes:

$$\vec{E} + \vec{v} \times \vec{B} = \eta \vec{J} \tag{3.1.3}$$

3.2 MHD equilibrium and instabilities

The MHD model can describe a wide range of dynamical properties, such as equilibrium and its stability, of a wide range of plasmas, from astronomical to laboratory ones. In order to study plasma equilibrium, the assumptions of stationary state and static plasma are needed, which means that all the physical quantities do not depend on time and the velocity field is considered $\vec{v} = 0$. Usually, also the electric field $\vec{E}$ is considered as zero (quasi-neutrality).
Introducing these assumptions in the ideal MHD model, after some algebrical steps the force-balance equation can be obtained [12]:

$$\vec{\nabla} p = \vec{J} \times \vec{B} \tag{3.2.1}$$

This equation tells that the pressure tries to move the plasma from hot to cold regions while the Lorentz force opposes this tendency and generates the magnetic confinement.
Another interesting information given by this equation is that J and B are perpendicular to the gradient of pressure. So they must lie on surfaces at a constant value of p wound around the magnetic axis, the so-called magnetic surfaces.

Another way to see the equation 3.2.1, is to substitute this equation in the Ampére law $\vec{\nabla} \times \vec{B} = \mu_0 j$, in order to obtain the pressure-balance equation:

$$\vec{\nabla}\left(p + \frac{B^2}{2\mu_0}\right) = \frac{1}{\mu_0}(\vec{B} \cdot \vec{\nabla})\vec{B} \tag{3.2.2}$$

All the algebraic steps can be found in [11].
In the left side there is the pressure, which is the sum of the kinetic pressure and a magnetic pressure, and in the right side a term which is connected to the bending of the magnetic field lines. When the magnetic field lines are bent the system tries to return to the original configuration due to the presence of a magnetic tension that contributes to the total pressure.

When the equilibrium structure is clear, it is possible to move to a more important topic, the plasma instabilities, the ideal and the resistive ones. But in order to understand, an introduction to the concept of magnetic topology is needed.

3.2.1 Magnetic topology

In mathematics, topology is concerned with the properties of geometric objects that remain unchanged under continuous deformations, such as stretching and twisting. When we refer to magnetic topology, we mean the application of this type of studies to the magnetic field lines of a system.

The preservation of such properties can introduce some constrains on the dynamics of the system that can create new types of problems, called topological, that are very difficult to approach. If two magnetic configurations can be deformed one in the other in a continuous way, so without cutting and pasting the field line, then these two configurations have the same magnetic topology. In figure 3.2.1, it is possible see an example of the two different cases. Figures a and b have the same topology because the b can be obtained from the other by envelop the N circle on the M one. The figure c has a different topology because it is impossible to obtain it from a without cutting and pasting the field lines.

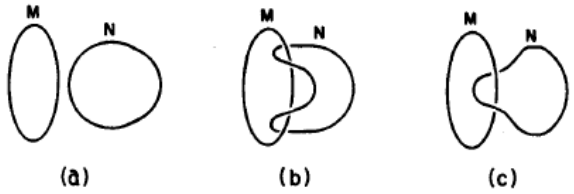

Figure 3.2.1: Three different configurations for two magnetic field lines. Figure a and b have the same magnetic topology, while c has a different one.

In the ideal MHD, in which the magnetofluid has zero resistivity, the induction equation (3.1.2) becomes the following:

$$\frac{\partial \vec{B}}{\partial t} = \vec{\nabla} \times (\vec{v} \times \vec{B}) \tag{3.2.3}$$

This equation has the same structure of the Kelvin's vorticity theorem, with the substitution of the vorticity ω with the magnetic field B. This analogue of the Kelvin's theorem takes the name of Alfvén theorem of the "magnetic flux freezing". The Alfvén theorem says that when the magnetic field satisfies the equation 3.2.3, the magnetic field lines are "frozen" inside the plasma: if the plasma column moves in the space, the magnetic field lines move with it. So, if two elements are connected by a field line they will always be connected independently of the behaviour of the plasma. This theorem is the key of the study of the magnetic topology of a system because it tells that the magnetic topology of a ideal MHD system cannot change. This is an important constrain of the dynamics of the system because it means that the system can only evolve trough magnetic configurations which are topologically equivalent.

3.2.2 Ideal instabilities

There are two destabilizing forces that can introduce instabilities inside a plasma, the one given by the presence of a gradient of current (Current-driven instabilities) and the one given by the gradient of pressure (Pressure-driven instabilities). β is a plasma parameter that can distinguish the two different cases. It is the ratio between the kinetic pressure and the magnetic pressure of a plasma. At low β, which means a well confined plasma, the driving force comes from the radial gradient of the toroidal current, instead, at high β the pressure gradient contributes to the instability too.

All these instabilities can be divided in two main groups: the ideal ones, which occur in a perfectly conductive plasma, and the resistive ones, which depend on the resistivity of the plasma. Due to the geometrical properties of the system, it is convenient to perform a Fourier transform of the angular coordinates. In this way, these instabilities can be decomposed in a infinite spectrum of Fourier modes, each one defined by a couple of integer numbers (m,n).

A (m,n) couple defines a precise helicity of the field lines: during the thesis, we will use the expression "wave helicity" referring to their magnetic mode.

Ideal instabilities are perturbations of the plasma equilibrium that cannot change the magnetic topology of the system. These instabilities are "ideal" in the sense that they would occur even if the plasma is perfectly conductive.
The safety factor q is an important parameter that gives information about the helical structure of the magnetic field.

$$q(r) = \frac{r}{R_0}\frac{B_\phi(r)}{B_\theta(r)} = -\frac{m}{n} \tag{3.2.4}$$

It represents the number of poloidal turns that the magnetic field lines do every single toroidal turn. The q behaviour has profound consequences in terms of plasma magnetohydrodynamic stability [3].
If the m/n ratio of a magnetic mode satisfies the equation 3.2.4, it is called resonant mode because it has the same periodicity of the magnetic field lines. The most common magnetic modes inside a toroidal plasma are all the ones with the poloidal magnetic number m=1. These are called kink modes: the plasma forms a single-helical structure along the toroidal axis.
For stability conditions, in a tokamak the q-value is always greater than 1. Instead, in RFP, the q-value is always lower than 1. In figure 3.2.2 this difference can be noticed.

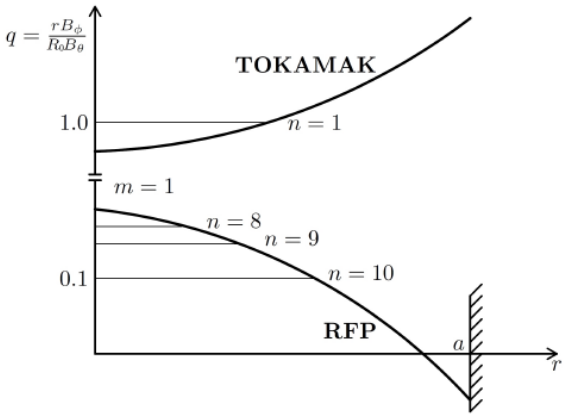

Figure 3.2.2: Comparison of the safety factor q radial profile between a Tokamak and a RFP devices [3].

3.2.3 Resistive instabilities

If the resistivity of the plasma is different from zero, the properties of the system change. The induction equation has the following shape, the one in the equation 3.1.2:

$$\frac{\partial \vec{B}}{\partial t} = \vec{\nabla} \times (\vec{v} \times \vec{B}) + \eta \nabla^2 \vec{B} \tag{3.2.5}$$

The Alfvén theorem is no more valid, making it possible to the magnetic field to change its own topology. In particular this is more visible when the term $\nabla^2 B$ becomes larger than the first one, so in presence of a large gradient of the magnetic field. Since large gradient of magnetic field corresponds to large current densities, due to Ampére's law, these regions are called current sheets. In these zones, it is possible the cutting and pasting of the field lines.

In figure 3.2.3, a schematic representation of a magnetic reconnection event is shown.

It the upper figure, the current sheet is defined by a dashed line which divides two regions where the magnetic field has two different directions. There, it is present a large gradient of the magnetic field, which means that the $\nabla^2 B$ term becomes relevant in the induction equation.
The magnetic field starts to diffuse in direction of the dashed line, from both the regions and they fuse together: this is the so-called magnetic reconnection event. This can create the typical magnetic islands, which are the circular structures that can be seen in the lower figure.
It is a loop process, in fact the decrease of the magnetic field in the two regions causes a reduction of the magnetic pressure, which is most relevant component of the total pressure in a high β plasma. The lowering of the pressure generates a force that tends to restore the initial configuration moving other magnetic field from other regions to the current sheet. So, while the field is lost in the current sheet, other new magnetic field is taken from the other regions in order to substitute it.

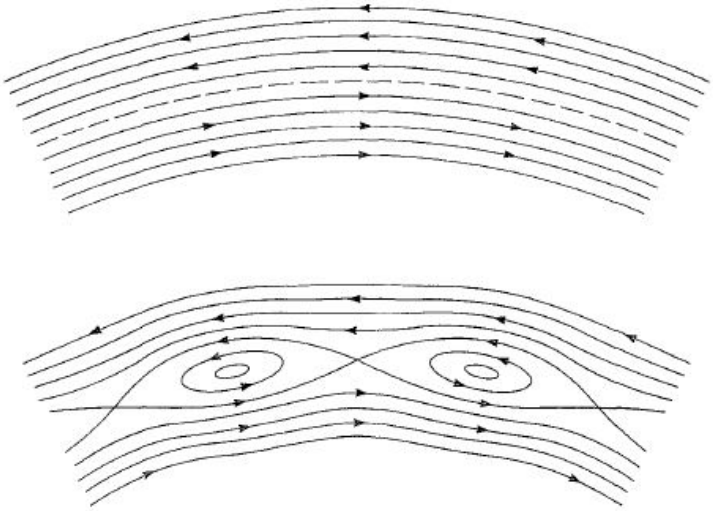

Figure 3.2.3: Schematic example of magnetic reconnection phenomena in a resistive plasma. The dashed line represents the current sheet. In the lower figure these is the representation of two magnetic islands of a tearing mode instability.

The interesting feature of the a reconnection event is the release of magnetic energy, converted in kinetic energy and thermal energy of the plasma. This can be observed by the acceleration of particles to very high velocities and the generation of waves and turbulence.
The solar flares, which are big explosions on the surface of the Sun with emission of high temperature plasma, are believed to be caused by magnetic reconnection events.
Resistive instabilities occur at surfaces with rational values of the safety factor q. At these surfaces the magnetic field lines break and reconnect to form magnetic islands as illustrated in figure 3.2.3. This instability takes the name of Tearing mode instability.

Another way to interpret this instability are the sawtooth oscillations. It is a periodic relaxation of the core temperature and density of the plasma. This can be explained through the value of the safety factor in the core, q_0. Usually the temperature of the core is increased by the ohmnic heating. This reduce locally the resistivity, which means an increasing of the current flow and a decreasing of q_0. When $q_0 < 1$, the resistive mode (m,n) = (1,1) becomes relevant and the sawtooth oscillations appear (figure 1.3.3). These oscillations make the core plasma to crash, mixing it with the external plasma, reducing the core temperature and returning to the initial configuration.

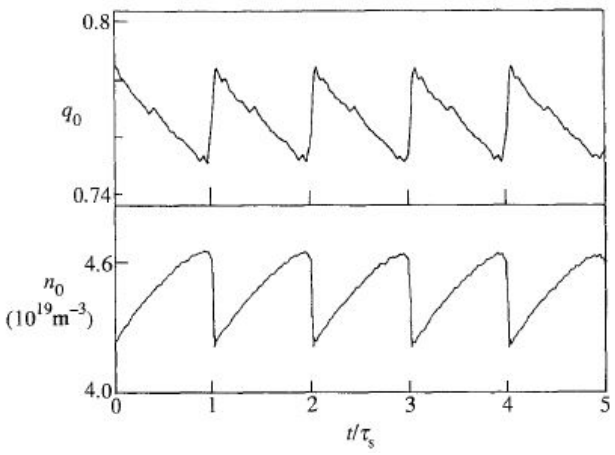

Figure 3.2.4: Time dependence of q_0 ans n_0 during sawtooth oscillations.

3.3 Alfvén waves

The Alfvén waves (AW), or hydro-magnetic waves, are a class of low-frequency waves that can be studied through the ideal MHD model. They are believed to be the carrier of the magnetic energy inside the plasma system [11].
Every type of wave has its own restoring force that generates the oscillating behaviour. In the case of AW there are two possible restoring forces: the one connected to magnetic tension $\frac{B^2}{\mu_0}$ and the other connected to pressure gradients. Due to this, there are two different groups of waves: the Shear Alfvén waves (SAW) and the Compressional Alfvén waves (CAW).

The SAWs can be generated by the magnetic tension. It's possible to imagine that magnetic tension acts on the magnetic field lines as the elastic tension acts on a stretch rope. When an external force tries to bend the rope, the elastic tension opposes to this force, trying to restore the equilibrium position. In the same way, the magnetic tension tries to cancel the effects of the magnetic perturbations on the magnetic lines, generating an oscillating motion. Figure 3.3.1 illustrates the behaviour of these types of waves.

Due to the parallelism with the elastic tension, it's possible to obtain the propagation velocity as the ratio of the tension, in this case the magnetic one, and the density ρ, as in the elastic case. The v_A is called Alfvén velocity:

$$v_A = \sqrt{\frac{B^2}{\mu_0 \rho}} \tag{3.3.1}$$

The CAWs, instead, are a mixture of two different types of waves: the acoustic and the magnetic waves. For this they are also called Magneto-Acoustic waves.
While in acoustic waves the pressure is generated by the only kinetic pressure, in CAWs the pressure has also a component connected to the presence of the magnetic field, called magnetic pressure $\frac{B^2}{2\mu_0}$. So, Alfvén waves are generated by both restoring forces: the propagation of these waves is related to the alternated compression and rarefaction not only of the plasma, but also of the magnetic field lines. In figure 3.3.1 the nature of CAWs is schematized.
The typical velocity of CAWs is given by:

$$v_M = \sqrt{c_s^2 + v_A^2}, \tag{3.3.2}$$

where $c_s = \sqrt{\frac{\gamma p_0}{\rho}}$ is the sound-speed, which is the velocity of the acoustic waves, and v_A the Alfvén velocity.

The CAWs can be also divided in two other different modes, called fast-mode and slow-mode. In the fast one, the restoring forces, which act on the system, are in phase making the wave propagate fast. In the other case, the forces are out of phase.

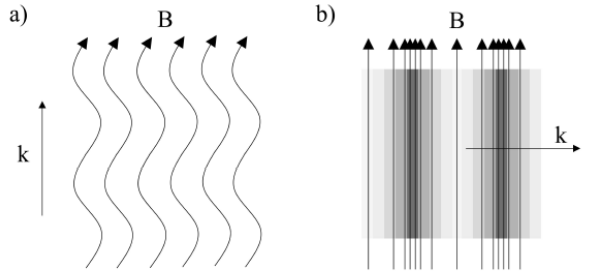

Figure 3.3.1: a) Shear Alfvén Waves (SAW). b) Compressional Alfvén Waves (CAW).

3.4 The SpeCyl code

SpeCyl is a code that numerically solves the equations of the visco-resistive MHD in cylindrical geometry (eq. 3.4.1), under some assumptions [13].
The first assumption is that the equations are solved in the limit of $\beta \to 0$, that corresponds to the assumption that the kinetic pressure of the plasma is negligible compared to the magnetic one. This assumption can be used to describe the dynamics of a strongly current-driven plasma like the one in the RFP configuration. Another assumption is on the mass density, which is considered stationary $\rho(r)$.

The resulting MHD equations are the following:

$$\begin{aligned}
&\vec{\nabla} \cdot \vec{B} = 0 \\
&\vec{\nabla} \times \vec{B} = \vec{J} \\
&\frac{\partial \vec{v}}{\partial t} + (\vec{v} \cdot \vec{\nabla})\vec{v} = \vec{J} \times \vec{B} + \nu \nabla^2 \vec{v} \\
&\frac{\partial \vec{B}}{\partial t} = \vec{\nabla} \times (\vec{v} \times \vec{B}) - \vec{\nabla} \times \eta \vec{J}
\end{aligned} \tag{3.4.1}$$

Thanks to the normalization described in section 2.2.1, the electrical resistivity η and the viscosity ν of the plasma become adimensional parameters. If we define the respective time scale of the two parameters, τ_η and τ_ν, it is possible to find a relation with the Lundquist number S and the magnetic Reynolds number R:

$$\begin{aligned}
\eta &= \frac{\tau_A}{\tau_\eta} = S^{-1} \\
\nu &= \frac{\tau_A}{\tau_\nu} = R_m^{-1}
\end{aligned} \tag{3.4.2}$$

The Lundquist number is defined as the dimensionless ratio between the Alfvén wave crossing time scale to the diffusion timescale, instead, the Reynolds magnetic number is the ratio between

the magnetic induction rate to the diffusion rate:

$$S = \frac{\mu_0 L v_A}{\eta} \qquad R_m = \frac{UL}{\eta} \tag{3.4.3}$$

where L is the typical length scale and U the velocity scale.

The last assumption of SpeCyl code is that viscosity and electrical resistivity are independent on time, but they have a radial profile of the form $A(r) = A_0\left(1 + ar^b\right)$, where A(r) is a generic quantity, A_0 its value in the center and a,b real numbers.
In particular were used: $a_\eta = 20$, $b_\eta = 10$ and $a_\nu = 0$.

3.4.1 Fouries modes

An helpful way to describe quantities in cylindrical geometry is to apply the Fourier's transform along the angular directions θ and ϕ, obtaining the decomposition of the quantity in Fourier's modes (m,n). The SpeCyl code adopts this description as well : it returns the Fourier components of the magnetic and velocity field for a set of magnetic modes (m,n), as a function of time: $B_j^{m,n}(r,t)$ and $v_j^{m,n}(r,t)$ (for $j = r, \theta, \phi$).

From these values it is possible to reconstruct a single component of the field in the real space using an Fourier anti-transform:

$$B_j(r,\theta,\phi,t) = \sum_{m=-M}^{M} \sum_{n=-N}^{N} B_j^{m,n}(r,t) e^{i(m\theta + n\phi)} \tag{3.4.4}$$

There are two important assumptions to do on the last equation. The first one is to assume that $B_{-m,-n} = B^*_{m,n}$, where * indicates the complex conjugate. This guarantees to work with real quantities such as every physical quantity. The second one is the values of the M,N quantities, which define the spectrum of Fourier modes that are considered. From the mathematical point of view, those numbers should be very large in order to obtain a very precise result. But, from a physical point of view, they should be a compromise between interesting results and computational costs.

The selected ranges of M,N values are the ones that resonate with the safety factor q(r) near the axis. Observing figure 1.3.3 and considering an aspect ratio similar to the RFX-mod experiment, it is possible notice that one of most unstable modes is the (m,n) = (1,-8).
For this reason, the ranges were selected around the ratio m/n = 8 (figure 3.4.1):

- m=0 $\rightarrow$ n $\in$ [-25,0];
- m=1 $\rightarrow$ n $\in$ [-55, 10];
- m=2 $\rightarrow$ n $\in$ [-50,-5];
- m=3 $\rightarrow$ n $\in$ [-60,-15];
- m=4 $\rightarrow$ n $\in$ [-70,-25].

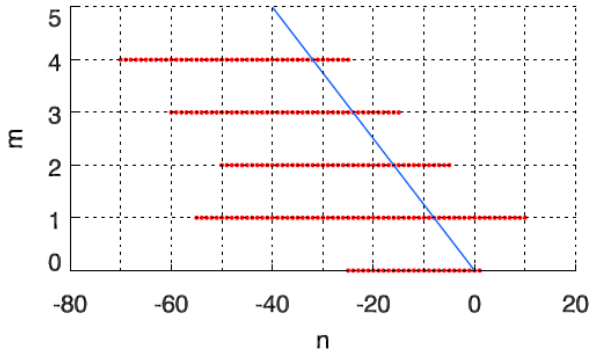

Figure 3.4.1: Spectrum of the calculated mode in a typical SPECYL simulation of an RFP plasma. The blue line represent the helicity h = m/n = 8.

3.5 SpeCyl dataset description

The Specyl simulation analyzed in this thesis has the following characteristics.
Plasma flow was taken to be vanishing at r=a. The boundary conditions admit a magnetic field not purely tangent to the shell, with an imposed radial component, i.e. helical boundary conditions on $B_r(a)$. The dissipation parameters (eq. 3.4.2) are $S = \frac{1}{\eta} = 10^6$ and $R_m = \frac{1}{\nu} = 10^6$.
The simulation time step is $10^{-4}\tau_A$ and fields were saved every $0.1\tau_A$.
The simulated plasma is considered composed by only hydrogen atoms.

In figure 3.5.1 and 3.5.2, there is the temporal dynamics of selected quantities coming from SpeCyl computation. It is shown the temporal evolution of the magnetic field radial components of the mode (0,0) and the mode (1,-7). From these pictures, two important considerations can be discussed.

The first one is on the field structure of the mode (0,0), the so-called axisymmetric mode. The particular feature of this mode is that it depends only on the radial coordinate r. This can be easily seen observing the equation 3.4.4 and introducing the fact that m=n=0.
As consequence of $\vec{\nabla} \cdot \vec{B} = 0$, the $B_r^{0,0}(r)$ component must be zero everywhere.
The axisymmetric mode is what we call "equilibrium field" in the modelling of ion heating (section 2.2). Actually, observing the figure 3.5.1, it is possible to notice that it is not perfectly constant in time. For the test-particle simulation, it has been taken at a fixed temporal instant inside the reconnection event, in order to remove the temporal dependence.

The second consideration is about the behaviour of the mode (m,n) in the temporal window of $[38600,39100]\tau_A$, evidenced by the blue dashed lines. These rapid changes and multiple oscillations of the magnetic field components are a clear signal of the presence of a magnetic reconnection event. This is an example of a typical temporal window that will be described in the section 3.6.1.

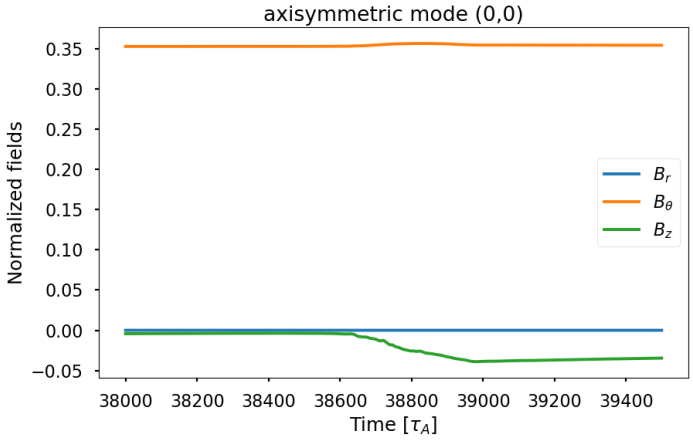

Figure 3.5.1: Magnetic field temporal evolution of the axisymmetric mode (0,0) in the radial position r/a=0.9, performed by the SpeCyl code. It is important to notice that $B_r^{0,0} = 0 \ \forall t$.

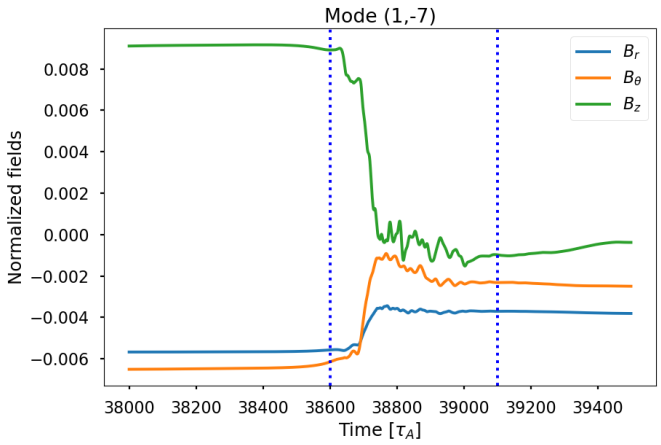

Figure 3.5.2: Magnetic field temporal evolution of the mode (1,-7) in the radial position r/a=0.9, performed by the SpeCyl code. A magnetic reconnection event is evidenced by the two blue vertical dashed lines. These lines define also the temporal window used for the FFT (section 3.6.1).

3.5.1 Pre-processing of SpeCyl data

In order to learn the structure of the simulation's data and, at the same time, obtain some quantities that may be useful in the other sections, some preliminar calculations were performed.

The goal of these exercises is to study the structure of the Fourier space and to learn how it is connected to the real space. One of the most important properties of the Fourier space is the non-linearity of the product of variables. This is called convolution, which tells that a non-linear variable in the real space is given by the infinite sum of all the possible combinations of the modes of that variables in the Fourier space.
In these exercises we will show how the convolution can make the computation of relevant quantities, such as the magnetic energy and the electric field, more difficult to approach.

If we define two real variables, as B_i and v_j, and we also define their Fourier decomposition following the definition of the equation 3.4.4 considering respectively the modes (m,n) and

(m',n') for the two variables, their product is given by the following equation:

$$v_j B_i = \sum_{\tilde{m},\tilde{n}} \left(\sum_{m,n} B_i^{m,n} v_j^{\tilde{m}-m,\tilde{n}-n} \right) e^{i(\tilde{m}\theta + \frac{\tilde{n}z}{R_o})} \tag{3.5.1}$$

$$(v_j B_i)_{\tilde{m},\tilde{n}} = \sum_{m,n} B_i^{m,n} v_j^{\tilde{m}-m,\tilde{n}-n} \tag{3.5.2}$$

in which

$$\tilde{m} = m' + m \qquad \tilde{n} = n' + n \tag{3.5.3}$$

The full derivation of this equation can be found in the appendix A.4.
The equation 3.5.1 tells that the element $[B_i v_j]_{\tilde{m}\tilde{n}}$, which is a single mode $(\tilde{m}, \tilde{n})$ of a product of two variables in the real space, is given by the sum of the all possible products of the two variables with such modes (m,n) and (m',n') that satisfy the particular condition 3.5.3. But in order to obtain the product of the real variables, equation 3.5.1, it is necessary to sum over all the possible couples $(\tilde{m}, \tilde{n})$.

Given the i-th component of the magnetic field by the equation 3.4.4, in order to compute the magnetic energy it is necessary to calculate the product of the i-th component with itself, due to the definition

$$E_m = \frac{B^2}{2\mu_0} = \frac{1}{2\mu_0} \sum_{i=1}^{3} B_i B_i \tag{3.5.4}$$

This can be done using the equation 3.5.1, with twice the same field component B_i instead of different ones. The resulting equation takes the form:

$$B_i B_i = \sum_{\tilde{m},\tilde{n}} \left(\sum_{m,n} B_i^{mn} B_i^{\tilde{m}-m,\tilde{n}-n} \right) e^{i\left(\tilde{m}\theta + \frac{\tilde{n}z}{R_0}\right)} \tag{3.5.5}$$

From the computational point of view, the problem is the calculation of all the possible combination of m,m' and n,n' that satisfy the equations in 3.5.3. The complete range of (m,n) values used for this computation is the one defined in the section 3.4.1.
The computational trick is to fix a value for $\tilde{m}$ and $\tilde{n}$, compute all the possible couples (m,m') and (n,n') that satisfy the equation 3.5.3 and than translate them in terms of B,v products. A python code was developed in order to compute this calculations.

The computation of the electric field starting from the magnetic field given by the simulation needed some more computational steps. The idea was to use the Ohm's equation, computing the two terms separately:

$$\vec{E} = -\vec{v} \times \vec{B} + \eta \vec{\nabla} \times \vec{B} \tag{3.5.6}$$

They are two cross products in cylindrical coordinates. The second one, which is the curl of the magnetic field, is the simpler term to compute because it does not contain products of variables, but only spatial derivatives of the magnetic field. In cylindrical coordinates, it has the form:

$$\vec{\nabla} \times \vec{B} = \begin{bmatrix} \frac{1}{r}\frac{\partial B_z}{\partial \theta} - \frac{\partial B_\theta}{\partial z} \\ \frac{\partial B_r}{\partial z} - \frac{\partial B_z}{\partial r} \\ \frac{1}{r}\left(\frac{\partial (r B_\theta)}{\partial r} - \frac{\partial B_r}{\partial \theta}\right) \end{bmatrix} \begin{bmatrix} \hat{r} \\ \hat{\theta} \\ \hat{z} \end{bmatrix} \tag{3.5.7}$$

The other term, instead, has a lot of products of variables in Fourier space.

As in the previous step, the cross product can be developed in the following shape:

$$\vec{v} \times \vec{B} = \begin{bmatrix} B_z v_\theta - B_\theta v_z \\ B_r v_z - v_r B_z \\ B_\theta v_r - B_r v_\theta \end{bmatrix} \begin{bmatrix} \hat{r} \\ \hat{\theta} \\ \hat{z} \end{bmatrix} \tag{3.5.8}$$

All the products inside this equation have to be computed with the related version of the equation 3.5.1. It must be applied in the same way of the calculation of the magnetic energy.
Once performed all these steps, the electric field was computed as the sum of the two parts.
The convolution is the principal reason of why we will work in the real space in the following sections.

3.6 Alfvénic turbulence extraction from SpeCyl simulation

The main parameters of the Alfvén waves that are required in order to apply the modelling of ion heating are the frequency of the wave, the wave vector and its amplitude. These quantities are needed to complete the vector potential of equation 2.2.3.
The three parameters need different types of calculations, which will be described in the following pages. The amplitude is computed starting from the original magnetic field given by the SpeCyl simulation, while the frequency and the wave vector are derived from the perpendicular component of the field respect to the direction of the equilibrium field component.
The parallel field has be neglected simply because the other component showed more defined peaks in the spectrograms. In this way, it was possible to avoid errors due to the peaks selection.

Before starting with any type of calculation, the first step is to translate the SpeCyl data from the Fourier space to the real space, using the Fourier anti-transform of the magnetic field. This is necessary in order to obtain a real signal $\vec{B}(r, \theta, \phi, t)$ which is more easy to be studied and analyzed.

The complete anti-transform of the j-component ($j = r, \theta, z$) of the field is given by:

$$B_j(r, \theta, \phi, t) = \frac{1}{2} \sum_{m,n} \left[B_j^{m,n}(r,t) e^{i(m\theta + n\phi)} + \overline{B_j^{m,n}(r,t)} e^{-i(m\theta + n\phi)} \right] \tag{3.6.1}$$

$B_j(r, \theta, z, t)$ is the j-th component of the total magnetic field. This equation is clearly a sum over all the possible modes of terms, that are the sum between a complex number and its conjugate, indicated by the over-bar. This is done in order to obtain a real magnetic field, which is the one that we usually measure in the experiments. In order to apply this equation it is necessary the definition of the two angular variables θ, ϕ in a specified range, usually $[0, 2\pi]$.

If it necessary to compute the j-th field component of a single mode (m,n), the equation 3.6.1 reduce to the following one:

$$B_j^{m,n}(r, \theta, \phi, t) = \frac{1}{2} \left[B_j^{m,n}(r,t) e^{i(m\theta + n\phi)} + \overline{B_j^{m,n}(r,t)} e^{-i(m\theta + n\phi)} \right] \tag{3.6.2}$$

At this point, the basic idea is to divide the magnetic field of the mode (m,n) in two different components, one parallel to the equilibrium magnetic field and the other perpendicular to it. This method allows to distinguish the two fundamental directions inside the cylindrical structure. In order to do this, the versor of the equilibrium field was computed as the ratio between the field components and the modulus of the field:

$$\hat{B}_j^{0,0}(r, \theta, \phi) = \frac{B_j^{0,0}(r, \theta, \phi)}{|B^{0,0}(r, \theta, \phi)|} \tag{3.6.3}$$

Given the versor, the computation of the $B_{\parallel}^{m,n}$ and $B_{\perp}^{m,n}$ is easily performed by using the following relations:

$$\begin{aligned} B_{\parallel}^{m,n}(r,\theta,\phi,t) &= \vec{B}^{m,n}(r,\theta,\phi,t)\cdot\hat{B}^{0,0}(r,\theta,\phi) \\ B_{\perp}^{m,n}(r,\theta,\phi,t) &= \left[\vec{B}^{m,n}(r,\theta,\phi,t)\times\hat{B}^{0,0}(r,\theta,\phi)\right]\times\hat{B}^{0,0}(r,\theta,\phi) \end{aligned} \tag{3.6.4}$$

The same process was also applied to the velocity field, using the equilibrium velocity field and obtaining $v_{\parallel}^{m,n}(r,\theta,\phi,t)$ and $v_{\perp}^{m,n}(r,\theta,\phi,t)$.

3.6.1 Study of the wave frequency spectrum

Once given the magnetic signal as a function of time, it is possible to apply to it a fast Fourier transform (FFT) in time in order to obtain the spectrogram of the signal.
A spectrogram is a graph that displays the strength of a signal over time (or space) for a given frequency range. Using a color spectrum, it points to the frequencies where the signal's energy is highest. This is usually done to observe which are the fundamental frequencies that compose the signal itself.

The FFT algorithm needs a temporal window of the signal in which to be applied. For every magnetic mode (m,n), we want to apply the FFT to temporal section connected to the magnetic reconnection events.
In figure 3.5.2, it is possible to observe an example of temporal window selection for the magnetic mode (1,-7). It is possible to see that there is not a precise way to define a temporal window, because the magnetic reconnection event has not a defined duration. But at the same time, we are interested in define a time order of magnitude of the event. Analyzing and comparing a large spectrum of magnetic modes, we can conclude that the event has a duration in the range of $[500, 700]\tau_A$. An average temporal window of $600\tau_A$ has been selected and applied to each magnetic mode.

The spectrograms have been computed for every magnetic mode with m=0 and m=1, because they are the ones with the higher amplitudes.
The picture 3.6.1 represents the spectrogram of the magnetic and the velocity $\perp$ and $\parallel$ field components of the magnetic mode (1,0).
It is possible to note that most of the information can be found at low frequency. The perpendicular component of the fields seems to be composed by a more spread set of frequencies than the respective parallel component. It is also possible to notice that only in the $B_{parallel}$ component there is no a power distribution along the radial direction, but it seems to be almost uniform.

From the spectrograms it is possible to extract the main frequencies that compose the original signal at a fixed radial position. Following the structure of the radial mesh, 100 different radial positions have been analyzed singularly (one for each position on the mesh), extracting one plot of power spectrum and frequency for each position.
Each one of these plots has been submitted to a self-made python code that finds the most relevant power peaks at low-frequency and saves them.
Following this computation, the radial profiles of the frequency of the most important peaks have been obtained for each magnetic mode. It was noticed that the frequency of single peak did not change much along the radial direction. For this reason it was decided to assume the frequency as a constant, independent of the radius.

The picture 3.6.2 shows the power-frequency plot extracted from the spectrogram at a fixed radial position $r/a = 0.9$. The orange crosses highlight the peaks of the power spectrum under

the threshold $\tilde{\omega} < 1.0$. We decided to select only the first peaks for two principal reasons, the first is that they correspond to low-frequency waves ($\approx 10^5 Hz$) in the Alfvénic range, the second is that their power is the highest one.

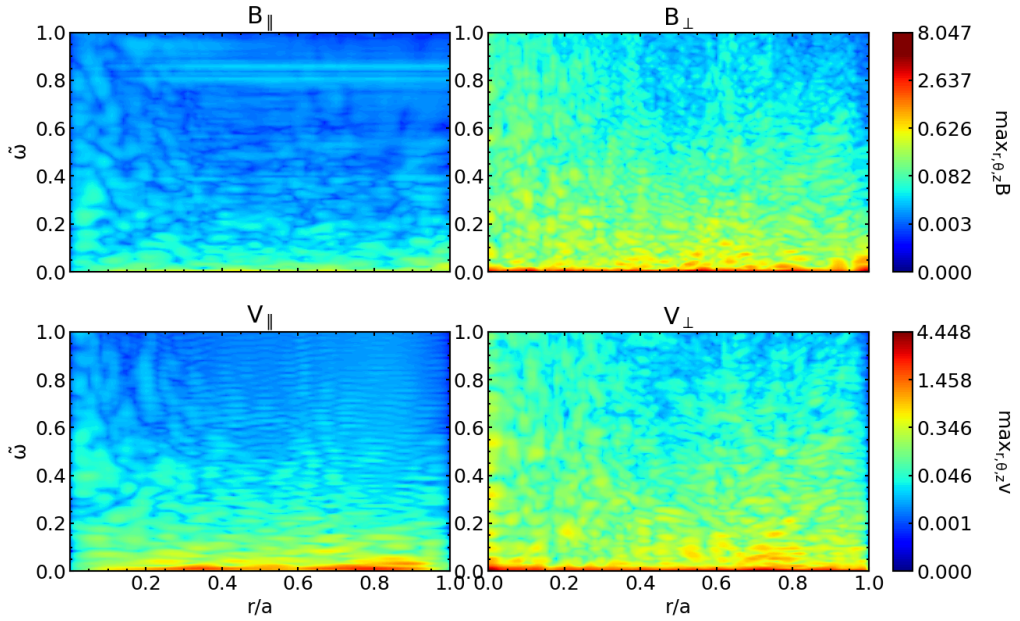

Figure 3.6.1: Spectrogram of the parallel and perpendicular components of velocity and magnetic fields of the magnetic mode (1,0). The colorbar on the right shows the meaning of the colors: the red highlights the presence of high power peaks. All the plots show the presence of an high low-frequency content distributed all along the radial direction.

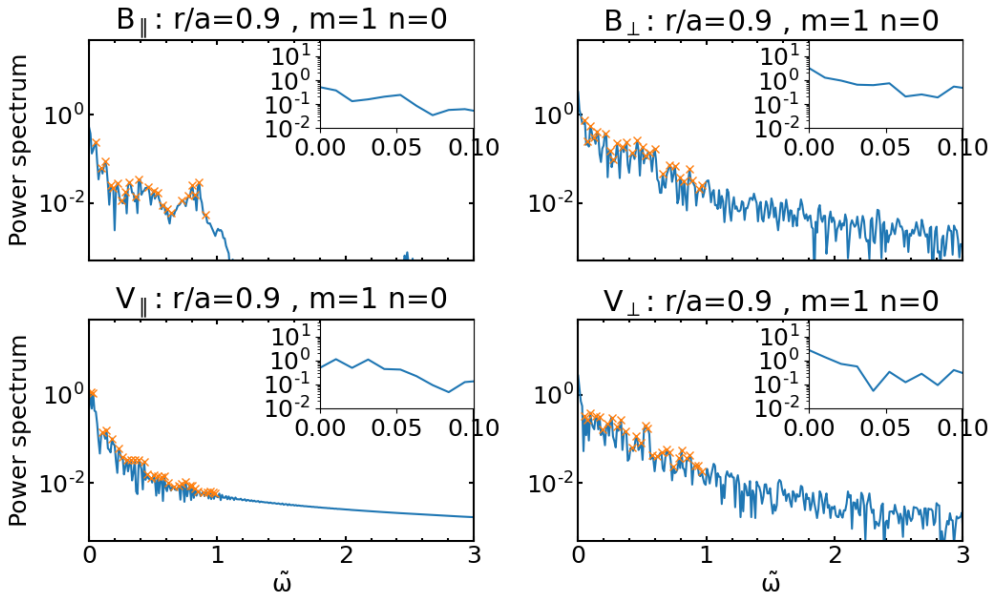

Figure 3.6.2: Power spectrum-frequency plots of the perpendicular and parallel components of magnetic and velocity fields of the mode (1,0) computed at radial position r/a = 0.9. The orange crosses highlight the power peaks selected by the python code, under the $\tilde{\omega} < 1$ threshold. The small figure on the right of the plots are zooms of the $[0,0.1]\tilde{\omega}$ region. It is possible to notice that the $\perp$ components have more energetic peaks than the respective $\parallel$ ones, at same frequency.

3.6.2 Derivation of the wave vector

The wave vector describes how many radians a wave passes per unit distance, related to the wavelength λ through the relation $k = \frac{2\pi}{\lambda}$.
Let us consider a wave vector k of a single wave which is travelling in the θ and z directions, while having m oscillations in the θ one and n in the z one, during a complete lap around the torus. This $\vec{k}$ will have the following shape:

$$\vec{k} = k_r\hat{r} + rk_\theta\hat{\theta} + k_z\hat{z} \tag{3.6.5}$$

Thanks to the application of the Fourier transform along the angular coordinates, the angular components of $\vec{k}$ become:

$$\begin{aligned} k_\theta &= \frac{2\pi}{\frac{2\pi r}{m}} = \frac{m}{r} \\ k_z &= \frac{2\pi}{\frac{2\pi R_0}{n}} = \frac{n}{R_0} \end{aligned} \tag{3.6.6}$$

where R_0 is the major radius of the RFX-mod experiment (table 1).
The reasons of this type of result can be found in the appendix A.3

The computation of the radial component k_r instead is more complicated. It cannot be derived from simple relations, but it must be computed from the simulation data.
The basic idea is to create two signals S_r and S_{r+dr} defined as following:

$$\begin{aligned} S_r^{m,n}(r,t) &= \sum_j a_j^{m,n}(r)e^{i\omega_j^{m,n}(r)t} \\ S_r^{m,n}(r+dr,t) &= \sum_j a_j^{m,n}(r+dr)e^{i\omega_j^{m,n}(r+dr)t} \end{aligned} \tag{3.6.7}$$

These equations represent the Fourier anti-transformation of the perpendicular component of the magnetic field mode (m,n) at different radial positions.
$S_r^{m,n}(r,t)$ represents the perpendicular component of the magnetic mode (m,n) at position r, and it is defined as the sum over all the j-peaks of the correspondent amplitude-frequency plot of the product between $a_j^{m,n}(r)$, which is the amplitude of the j-peak at r position, and $e^{i\omega_j^{m,n}(r)t}$ term, in which $\omega_j^{m,n}(r)$ is the frequency of the j-peak in the same position.
$S_{r+dr}^{m,n}(r+dr,t)$ represents the same signal computed in a radial position which differs from the first one by a factor dr, a single step of the radial mesh.

As we will see, from the phase difference between the two signals it is possible to computed the radial k_r of the wave.
In order to simplify the computation, only the first peak of every field component is introduced in the equations 3.6.7. This is a quite good approximation because the first peak's amplitude is always the dominant one.

$$\begin{aligned} S_r^{m,n}(r,t) &= a_1^{m,n}(r)e^{i\omega_1^{m,n}(r)t} \\ S_r^{m,n}(r+dr,t) &= a_1^{m,n}(r+dr)e^{i\omega_1^{m,n}(r+dr)t} \end{aligned} \tag{3.6.8}$$

From section 3.6.1, a simplification can be introduced: the frequency can be considered constant along the radial direction, so $\omega_1^{m,n}(r) = \omega_1^{m,n}(r+dr)$.

At this point, it is assumed that these signals are given by the propagation of a wave with wave vector k_r. In order to obtain a plane-wave description, we have to introduce the factor

$e^{ik_r r}$ in the signal. So, we decided to identify the phase of the complex number $a^{m,n}(r)$ as the plane-wave term. It is possible to rewrite the previous equations in a new shape:

$$\begin{aligned} S_r(r,t) &= |a^{m,n}(r)|e^{i\phi}e^{i\omega^{m,n}(r)t} \\ S_r(r+dr,t) &= |a^{m,n}(r+dr)|e^{i\phi'}e^{i\omega^{m,n}(r)t} \end{aligned} \tag{3.6.9}$$

in which $\phi = k_r r + \Delta$ and $\phi' = k_r(r+dr) + \Delta$. k_r and Δ (generic phase) must be the same in the two signals because they represent the propagation of the same wave.

Combining the two signals, it is possible to obtain the wave vector k_r.
The first step is to define two new quantities:

$$\begin{aligned} G_r &= \frac{S_r(r,t)}{|a^{m,n}(r)|}e^{-i\omega^{m,n}(r)t} = e^{i\phi} \\ G_{r+dr} &= \frac{S_r(r+dr,t)}{|a^{m,n}(r+dr)|}e^{-i\omega^{m,n}(r)t} = e^{i\phi'} \end{aligned} \tag{3.6.10}$$

By applying the natural logarithm to the ratio of these two quantities it is possible to obtain the k_r term:

$$\frac{G_{r+dr}}{G_r} = \frac{e^{i\phi'}}{e^{i\phi}} = \frac{e^{i(k_r\cdot(r+dr)+\Delta)}}{e^{i(k_r\cdot r+\Delta)}} \tag{3.6.11}$$

$$ln\left[\frac{G_{r+dr}}{G_r}\right] = i(\phi' - \phi) = ik_r dr \tag{3.6.12}$$

$$k_r = \frac{\Delta\phi}{dr} = \frac{d\phi}{dr} \tag{3.6.13}$$

This equation means that the wave vector k_r of the wave which is propagating from r to $r+dr$ is given by the variation of the phase of the wave along the same direction, which coincide with the definition of space derivative of the phase.

3.6.3 Computation of the wave amplitude

As described in the section 2.2, the wave amplitude corresponds to the vector potential of the magnetic field of the perturbation.
The vector potential $\vec{A}$ of the magnetic field can be computed knowing that its curl corresponds to the magnetic field:

$$\vec{B} = \vec{\nabla} \times \vec{A} \tag{3.6.14}$$

Developing this equation in cylindrical coordinates, a system of 3 non-linear differential equations is obtained. This represents the cylindrical components of the magnetic field as a function of the components of the vector potential:

$$\begin{cases} B_r(r,\theta,z) = \frac{1}{r}\partial_\theta A_z(r,\theta,z) - \partial_z A_\theta(r,\theta,z) \\ B_\theta(r,\theta,z) = \partial_z A_r(r,\theta,z) - \partial_r A_z(r,\theta,z) \\ B_z(r,\theta,z) = \frac{1}{r}\left[\partial_r(rA_\theta(r,\theta,z)) - \partial_\theta A_r(r,\theta,z)\right] \end{cases} \tag{3.6.15}$$

It is possible to notice that even if the eq. 3.6.14 depends in general on the time, the system of 3.6.15 does not depend on it. In order to simplify the vector potential computation, it was decided to fix a single temporal instant in order to remove the time dependence.

In section 4.3, a full explanation of this choice is given.
The vector potential can be written as follows:

$$A(r,\theta,z) = \left[A_r(r)e^{i(m\theta-\frac{nz}{R_0})}, A_\theta(r)e^{i(m\theta-\frac{nz}{R_0})}, A_z(r)e^{i(m\theta-\frac{nz}{R_0})}\right] \tag{3.6.16}$$

In this way, the angular derivatives become very easy to compute and the exponential part can be simplified with the one given by the magnetic field component. The resulting system of linear equations becomes the following:

$$\begin{cases} B_r(r) = \dfrac{imA_z(r)}{r} + \dfrac{inA_\theta(r)}{R_0} \\ B_\theta(r) = -i\dfrac{n}{R_0}A_r(r) - \partial_r A_z(r) \\ B_z(r) = \dfrac{A_\theta(r)}{r} + \partial_r A_\theta(r) - im\dfrac{A_r(r)}{r} \end{cases} \tag{3.6.17}$$

A general property of the vector potential is that it does not change if the gradient of a generic scalar function is summed to it (Gauge invariance).

$$A'(r,t) = A(r,t) + \nabla\Phi \tag{3.6.18}$$

It was decided to choose the gauge that gives $A_r(r) = 0$ for every position. In this way the system is reduced from three variables to only two.

For the case $B_{0,0}$ the computation of eq. 3.6.17 becomes simpler:

$$\begin{cases} A_z^{0,0}(x_{j+1}) = A_z^{0,0}(x_j) - drB_\theta^{0,0}(x_j) \\ A_\theta^{0,0}(x_{j+1}) = dr\left[B_z^{0,0}(x_j) + A_\theta^{0,0}(x_j)(1-1/x_j)\right] \end{cases} \tag{3.6.19}$$

in which x_j is the j-th position of the radial mesh and dr in the mesh step, defined as $dr = x_{j+1} - x_j$.

In the more general case $B_{m,n}$, the $B_r(r)$ component is different from zero and this makes the resolution more difficult. After some computational steps, the final equations are the following:

$$\begin{cases} A_z^{m,n}(x_{j+1}) = \dfrac{x_{j+1}}{im}\left[B_r^{m,n}(x_{j+1}) - i\dfrac{n}{R_0}A_\theta^{m,n}(x_{j+1})\right] \\ A_\theta^{m,n}(x_{j+1}) = \dfrac{dr}{x_j}\left[x_j B_z^{m,n}(x_j) - A_\theta^{m,n}(x_j)\right] + A_\theta^{m,n}(x_j) \end{cases} \tag{3.6.20}$$

This system of equations, in which the 2 unknown quantities are the potential vector radial components, has been solved numerically. The numerical solution of the second equation was used to compute the first one.
The obtained data of the vector potential have been also checked inserting them in the equation 3.6.16 and reconstructing the magnetic field. It was compared with the original one in order to check the validity of the resolution method.

Chapter 4

Results

This chapter summarizes all the results obtained in this thesis. They will be divided in three different sections.
The first one is related to the SpeCyl post-processing (described in the previous chapter) in which the Alfvén waves parameters have been extracted from the simulation.
The second section shows the first results obtained simulating the interaction of a particle with a single low-frequency wave. Two different cases will be shown, the mode (1,-7) and the mode (1,-8). The heating will be studied as a function of the simulation length and the amplitude of the waves. In third section, simulations with different sets of waves will be presented. In this case, the heating will be studied varying the combination of waves. The mass dependency of the heating will be also explored. In the end, a possible interpretation of the ion heating is given by the study of the Hamiltonian of the particle.

4.1 Results of SpeCyl post-processing

During the thesis, more than 20 different magnetic modes have been analyzed singularly following the procedures described in chapter 3. All the obtained results are qualitatively similar, with some differences only in terms of wave amplitudes. For this reason, it was decided to show in this section only two of these modes: the modes (1,-7) and (1,-8). These modes have been selected due to their huge difference in terms of perturbation amplitude.

4.1.1 Computation of the wave frequency

The computation of the Alfvén waves parameters starts from the spectrogram analysis of the parallel and perpendicular components of the SpeCyl fields, described in section 3.6.1.
For the FFT, it is necessary to decide a temporal window that has to contain magnetic reconnection event. Due to the fact that the reconnection event does not have a well-defined duration, it was decided to select an average window of $600\tau_A$, that was applied to each magnetic mode.

The spectrograms, for these cases, revealed a low-frequency content in both velocity and magnetic fields of all the magnetic modes. In figures 4.1.1 and 4.1.2, the spectrograms of the magnetic modes (1,-7) and (1,-8) are shown. It is possible to see that, in both cases, the relevant part of the spectrogram is at frequency lower than $\tilde{\omega} < 0.1$ (that correspond to ~ 1 MHz).
This confirms the presence of a large spectrum of low-frequency waves during a magnetic reconnection event in the simulated RFP plasma. For the magnetic field components, the spectral content is distributed all along the radial direction, while in $v_\perp$ it is concentrated in the center of the cylinder.

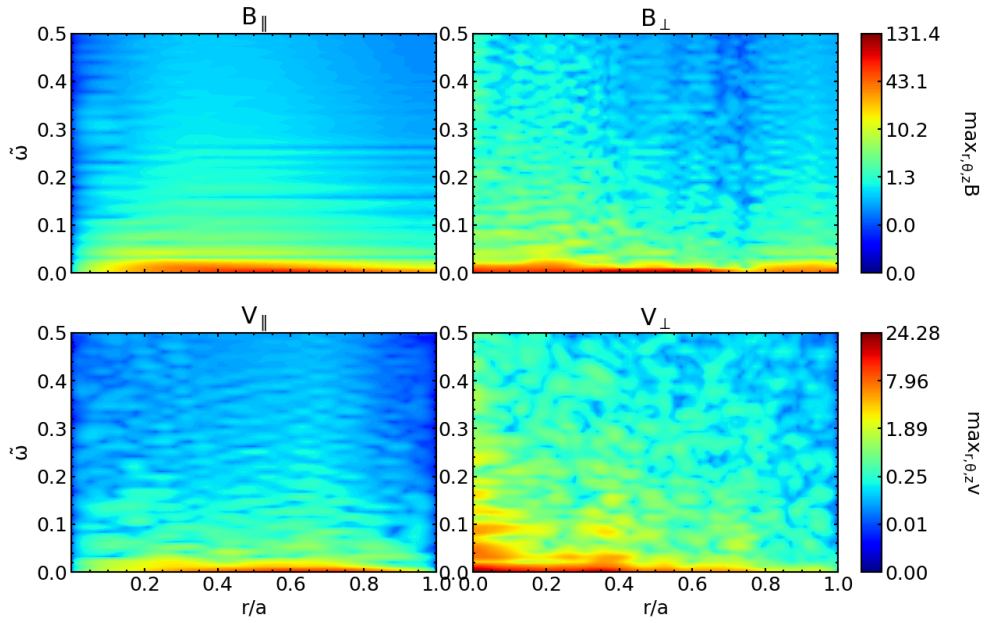

Figure 4.1.1: Spectrogram of the parallel and perpendicular components of velocity and magnetic fields of the magnetic mode (1,-7). The colorbar on the right shows the meaning of the colors: the red highlights the presence of high power peaks. All the plots show the presence of an high low-frequency content distributed all along the radial direction.

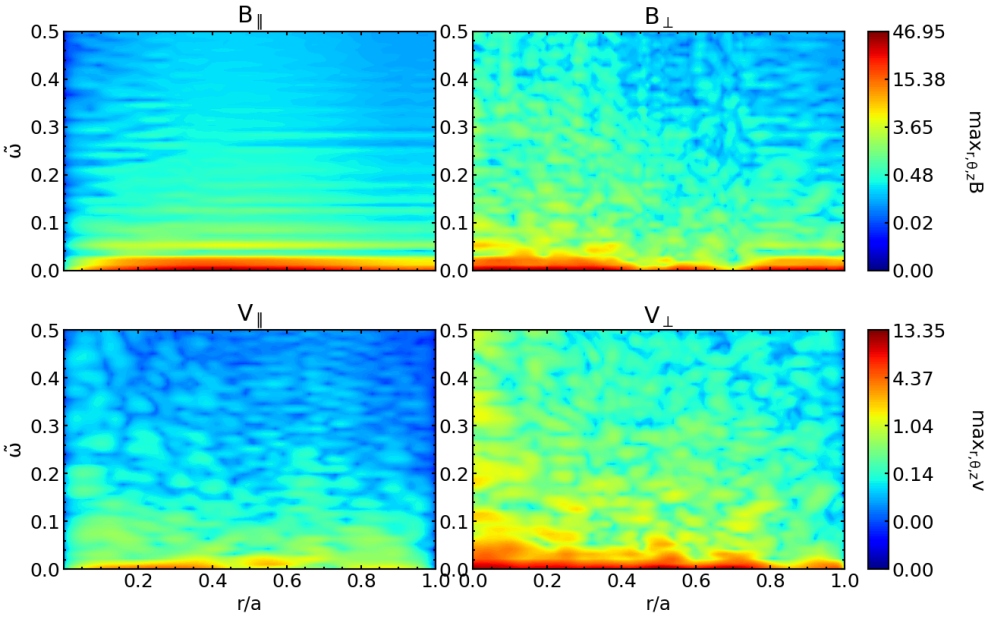

Figure 4.1.2: Spectrogram of the parallel and perpendicular components of velocity and magnetic fields of the magnetic mode (1,-8). The colorbar on the right shows the meaning of the colors: the red highlights the presence of high power peaks. All the plots show the presence of an high low-frequency content distributed all along the radial direction. $v_{parallel}$ seems to have the lower energy spectrum.

These spectrograms have been analyzed singularly as described in section 3.6.1. From each spectrogram, 100 different plots have been created by cutting the spectrogram at every radial

point of the mesh, spaced by 0.01 r/a. In this way it was possible to observe the behaviour of 2D power-frequency plots as a function of the radial position.
These graphs present a huge number of different power peaks which represent the most important Fourier components of the original signal. By using a built-in python function *scipy.find_peaks*, the amplitude and the frequency of the first 5 peaks for each plot has been saved.
In figures 4.1.3 and 4.1.4, the power-frequency plots at r/a=0.3 position of the two magnetic modes (1,-7) and (1,-8) are presented, for $\tilde{\omega} < 3$. The orange crosses correspond to the peaks found by the python code below a frequency threshold of $\tilde{\omega}_T = 1.0$. The small rectangle in the right of each plot is a zoom of the lowest frequency zone.

As an example, the frequency in SI units of the first peaks for the two magnetic modes (1,-7) and (1,-8) is:

$$\begin{aligned} \tilde{\omega}_{1st}^{1,-7} &= 0.042 \approx 6.2 \cdot 10^5 Hz \\ \tilde{\omega}_{1st}^{1,-8} &= 0.052 \approx 7.6 \cdot 10^5 Hz \end{aligned} \tag{4.1.1}$$

For the conversion in SI units, the Alfvén time τ_A can be computed by the using the experimental equation 2.2.20, with $n_e = 2.3 \cdot 10^{19} m^3$, $\gamma = 1$, $z = 1$ and $B = 1.3T$ which are the typical values of the RFX-mod experiment.
For an hydrogen plasma, the Alfvén time is: $\tau_A \approx 7.8 \cdot 10^{-8}$s. These frequencies have been compared with the ones in [14], in which the same SpeCyl simulation has been studied.
In the same way, it is possible to obtain the cyclotron frequency of an hydrogen ion by using the eq. 1.2.2: $\omega_c^H \approx 2.4 \cdot 10^7 Hz$.
So, comparing this result with eq. 4.1.1, it is possible to confirm that the considered waves have frequencies very lower than the resonance frequency (section 2.1).

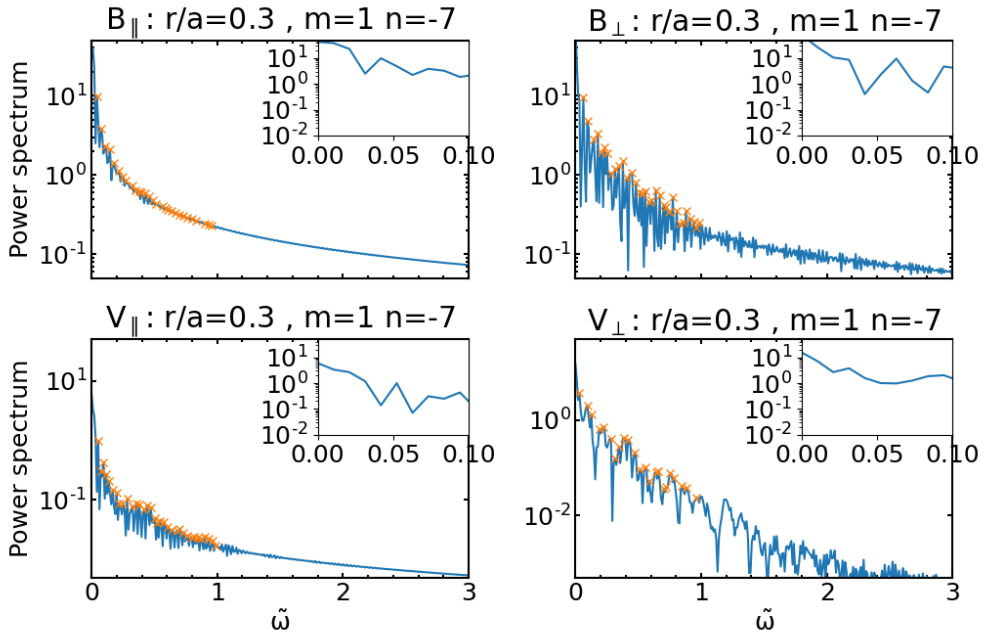

Figure 4.1.3: Power spectrum-frequency plots of the perpendicular and parallel components of magnetic and velocity fields of the mode (1.-7) computed at radial position r/a = 0.3. The orange crosses highlight the power peaks selected by the python code, under the $\tilde{\omega} < 1$ threshold. The small figure on the right of the plots are zooms of the [0,0.1]$\tilde{\omega}$ region.

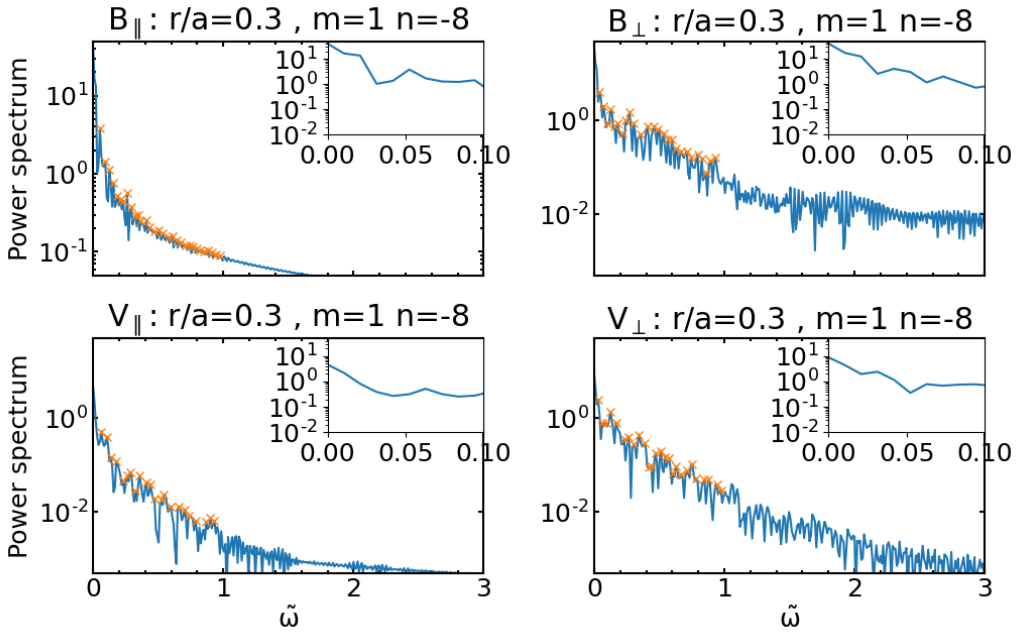

Figure 4.1.4: Power spectrum-frequency plots of the perpendicular and parallel components of magnetic and velocity fields of the mode (1.-8) computed at radial position r/a = 0.3. The orange crosses highlight the power peaks selected by the python code, under the $\tilde{\omega} < 1$ threshold. The small figure on the right of the plots are zooms of the [0,0.1]$\tilde{\omega}$ region.

4.1.2 Computation of the radial wave vector k_r

The next wave parameter, that was computed, is the wave vector $\vec{k}$. The angular components of this vector are already defined in the section 3.6.2 through geometrical considerations. The computation of the radial component is the only left. Applying the calculations of the section 3.6.2, the radial profile of the k_r component is performed for all the modes.

These calculations have shown several problems. One of the most important is related to the definition of the phase implemented in the python routine which was used. This routine computes the phase in the range $[-\pi, \pi]$. When the absolute value of the phase becomes higher than π, it is normalized again between $[-\pi, \pi]$. This can create big jumps of the phase that are catastrophic in the derivative computation (eq. 3.6.13).
For this reason, all the radial profiles of the phases have been analyzed and all the jumps have been corrected summing a term $\pm 2\pi$.
In figures 4.1.5 and 4.1.6, there is an example of this correction applied to the two example modes (1,-7) and (1,-8). In both cases, there are huge jumps of the phase: the (1,-7) mode presents a single jump at r/a = 0.3, while the other mode shows 5 jumps between [0.4,0.8]a. These jumps correspond to the enormous peak that can be seen at the same radial position in the respective right figures, blue curves. The orange curves are the ones corrected as described before. It is possible to see that the big jumps disappear.

Another problem is connected to the singular behaviour of the radial wave vector. It seems to oscillate around the $k_r = 0$ value, with a non-periodic high-amplitude oscillation. It can be seen in both right plots of 4.1.5 and 4.1.6. The rapid variation of this quantity can influence the behaviour of the Alfvén wave, changing its phase with a non-regular pattern (eq. 2.2.3).
In order to avoid this type of problem, it was decided to approximate the radial profile of k_r by

using a smoother function. In both cases, it was decided to use a sine function with an average amplitude. The red curves in the figures correspond to these functions. The precise analytical profile is the following:

$$k_r^{m,n}(r) = -\tilde{k}_{avg}^{m,n} \cdot sin(\omega_{avg}^{m,n} r) \tag{4.1.2}$$

k_{avg} corresponds to an average amplitude that was decided by observing the behaviour of the oscillations. Instead, ω_{avg} is the spatial frequency of the oscillation. It was decided to put as first approximation $\omega_{avg} = 2\pi$, making the wave vector to have a single period along the total radial direction.

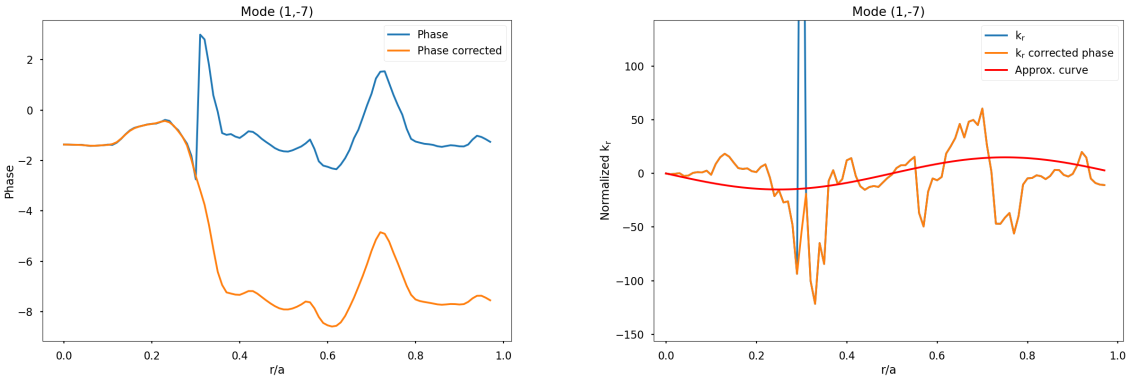

Figure 4.1.5: The left graph represents the radial profile of the phase difference between the two signals described in 6.3.3, computed for the mode (1,-7). On the right, the radial profile of k_r, which is nothing but the spatial derivative of the left graph. The red curve represents the approximation of the real plot. At $r/a \approx 0.3$ it is possible to see a jump of the phase described in 4.1.2.

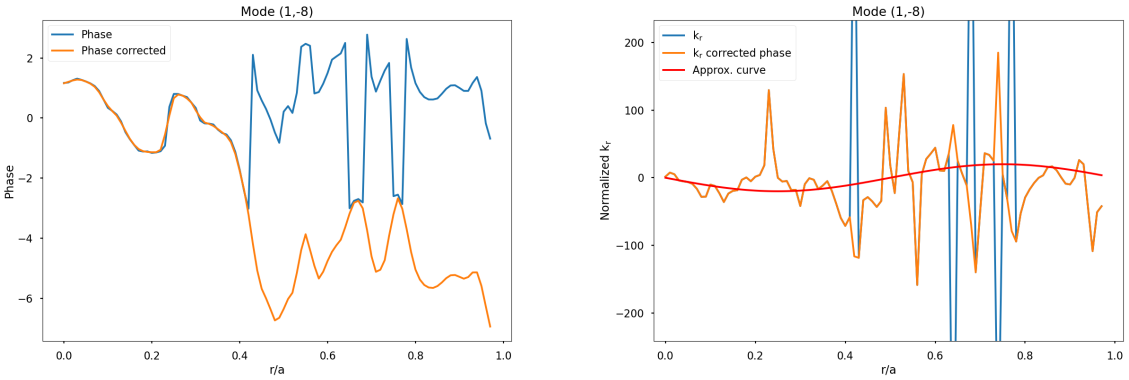

Figure 4.1.6: The left graph represents the radial profile of the phase difference between the two signals described in 6.3.3, computed for the mode (1,-8). On the right, the radial profile of k_r, which is nothing but the spatial derivative of the left graph. The red curve represents the approximation of the real plot. At $r/a \approx 0.4$ and between [0.6;0.7] it is possible to see many jumps of the phase described in 4.1.2.

The two average values used for the example modes (1,-7) and (1,-8) of the k_r-amplitude are:

$$\begin{aligned} \tilde{k}_{avg}^{1,-7} &= 10.0 \approx 22m^{-1} \\ \tilde{k}_{avg}^{1,-8} &= 20.0 \approx 44m^{-1} \end{aligned} \tag{4.1.3}$$

During the simulations, it was decided to try to change k_{avg} in order to understand how much it could influence the Alfvén wave behavior and how much we were modifying the system due to this approximation. It was observed that the k_r contribute to the phase of the wave was very small, so the approximation cannot change the final results too much.

4.1.3 Computation of the wave amplitude

The calculation on the Alfvén waves is the computation of the vector potential of the modes, which is connected to the wave amplitude. The calculations of the section 3.6.3 have been performed by a python code.
Due to the fact that the SpeCyl code computes the time evolution of the radial profile of the magnetic modes, it is necessary to choose a temporal instant in which compute the vector potential of the magnetic modes. It was decided to choose it in the middle of the magnetic reconnection event. Other points inside the reconnection temporal window show the same behaviour.

We recall that the results are obtained in the gauge that cancels the radial component of the vector potential. The radial profile of the axisymmetric vector potential components is presented in figure 4.1.7. The figures in 4.1.8 represent the vector potential of the example modes (1,-7) and (1,-8).
An important characteristic that can be observed in these figures is that the vector potential components (dashed lines) have a smooth radial profile. This is relevant during the simulation phase, in particular during the change of coordinates from the cylindrical ones to the cartesian ones. As described in section 3.2.2, this change is performed by interpolating the data of the vector potential. The smooth profile allows us to use a linear interpolation, which is the simpler and the faster type of interpolation. The second order interpolation, the parabolic one, was also performed. But it was not noted any difference between it and the linear one. Also for this reason, the linear interpolation was built into the code.

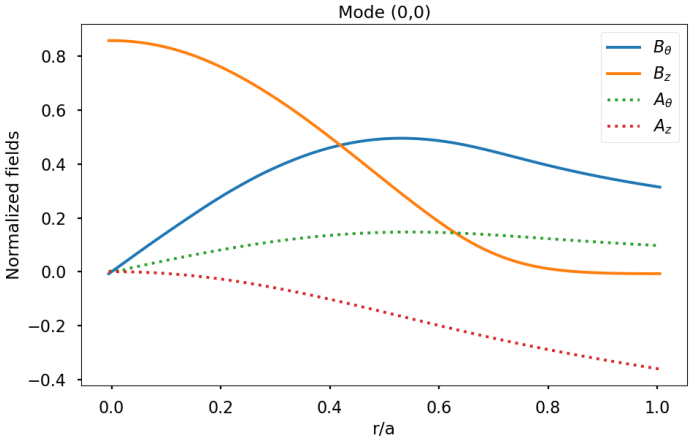

Figure 4.1.7: The radial profiles of the vector potential components of the axisymmetric field. With them, the magnetic field computed through this potential is superimposed to the initial magnetic field.

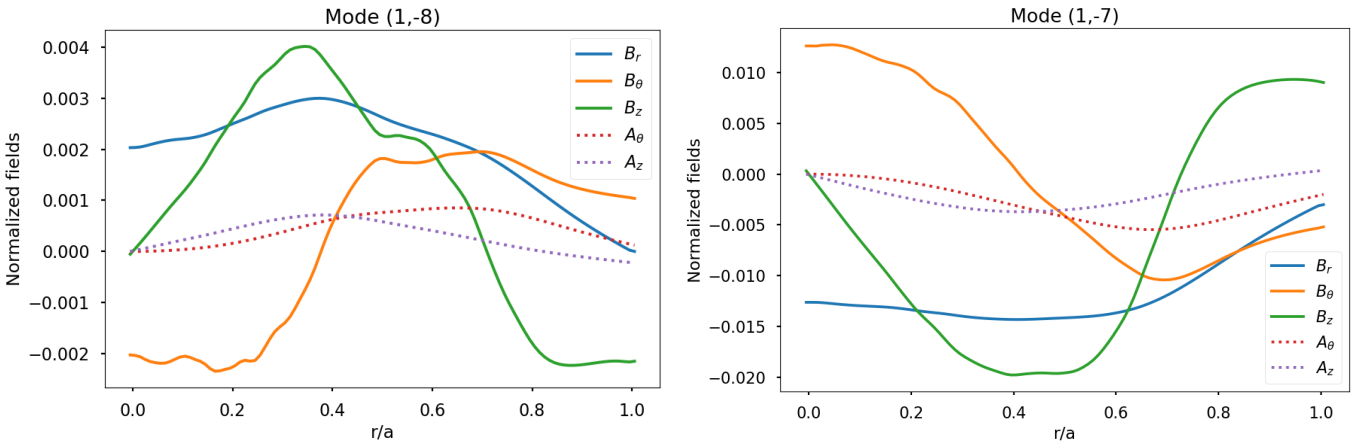

Figure 4.1.8: The two graphs represent the radial profile of the vector potential components of the two modes, 1,-8 on the left and 1,-7 on the right (dashed lines). With them, the respective magnetic field is plotted.

4.2 Simulations with a single low-frequency wave

A set of single-wave simulations has been performed for the magnetic modes (1,-7) and (1,-8) in order to better understand the dynamics of the system. We are interested in to study the temporal evolution of the test-particle energy, in particular to find evidences of energization. They have been performed for different times higher than $1000\tau_A$. It was decided to study some random simulation lengths before moving to the magnetic reconnection temporal window.

By observing the temporal evolution of the energy of the test-particles, it is possible to notice both cases of heating and not-heating. In figure 4.2.1, there is an example of this behaviour. In the first plot, there is the temporal evolution of a set of 4 particles, each starting in the same spatial point, but with different initial energies.
Consider this figure: from 0 to $300\tau_A$, the particles conserve their energies. This happens thanks to the shaping function $f(t)$ (figure 2.2.1), which acts as a perturbation-switch. It makes the perturbation to reach the its full amplitude around $300\tau_A$ and to start reducing at $1700\tau_A$. Without the perturbation, the particle moves inside an equilibrium field adiabatically. Between these limits, the particle starts to interact with the wave until the perturbation is switched-off and the system returns to the equilibrium. The particle energy oscillates with a sinusoidal-like shape from its initial energy to an higher one, and this amplitude of oscillation does not depend on the initial energy.
It is possible to see that there are many different possible results: the blue particle, with an initial energy of 4eV, returned to its initial energy, the yellow one, 24eV, lost energy in the interaction and the other two, 50eV and 73eV, gained different amounts of energy.

A similar structure can be observed in the second figure. In this case, particles with the same energy, 24eV, started their trajectory from different initial points. In this case, two particles had a strong heating while the others returned near to the original energy.

The statistical behaviour of these type of heating is clear. A particle can or cannot be heated, depending only by its initial conditions. To make the results significant from the statistics point of view, only the average energy gained by a set of independent simulations will be considered.

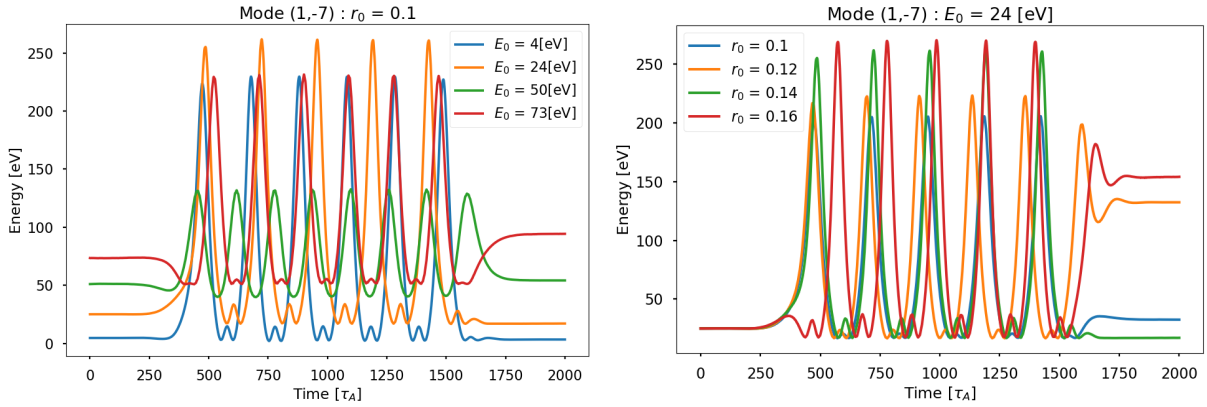

Figure 4.2.1: Temporal evolution of the energy fro two different sets of simulations. At left, 5 particles with different initial energies, but with the same initial position. At right, viceversa, same energies but different positions. In both cases, it is possible to note the increasing of the energy for some particles.

In figure 4.2.2, there is an example of the temporal evolution of another relevant variable, the squared modulus of the kinetic momentum. The simulation that it refers to is the red one that can be observed in the left figure of 4.2.1. The temporal behaviour of the kinetic momentum is clear. It is possible to see that the particle, which is in the equilibrium field in the first part of the simulation, changes the amplitude of the oscillation due to the interaction with the wave. At the end, after the wave disappears, the system return to an equilibrium configuration, but the momentum oscillates around an higher value, which is a clear evidence of energization.

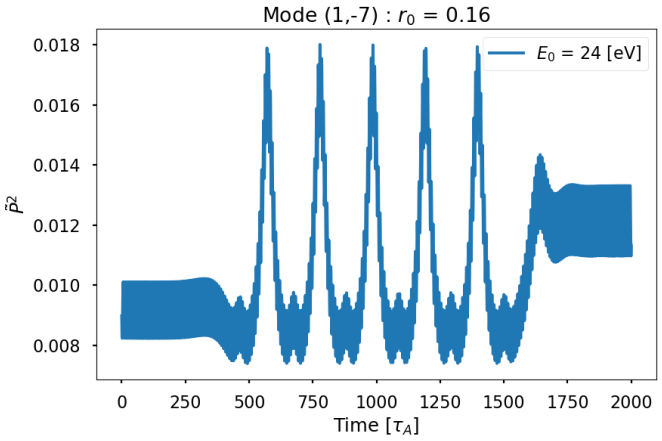

Figure 4.2.2: The squared modules of the kinetic momentum of a particle as a function of time. The difference between the initial and the final values evidences a relevant acceleration.

In figure 4.2.3, two examples of particle trajectory are presented in the xyz plane. On the left figure, it is possible to see the 3D trajectory of a particle inside the toroidal chamber with the only equilibrium field. While the particle rotates around the z-direction (toroidal direction), it makes a smaller (and faster) spiral rotation along the other directions. On the right picture, it is possible to observe the trajectory in the presence also of a low-frequency wave with helicity (1,-7). The perturbation modifies the regularity observed in the left figure introducing some irregularities in both the two spiral motions.

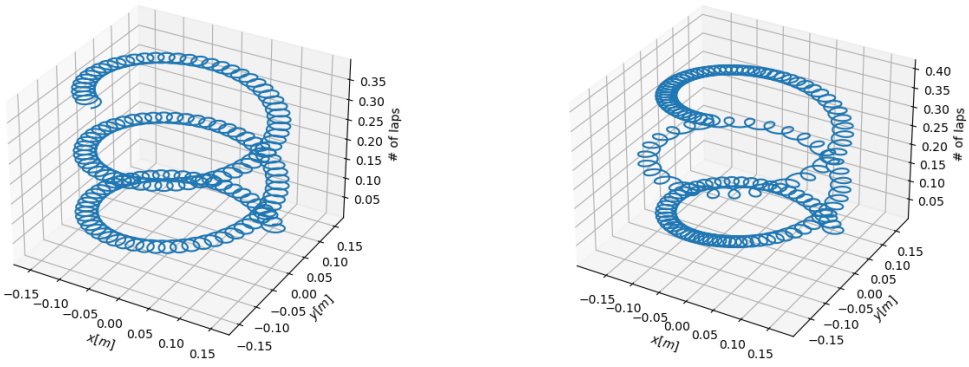

Figure 4.2.3: Trajectory of the particle in the xyz plane in two different conditions: in the presence of the only equilibrium field (left) and in the presence also of an Alfvén wave of the mode (1,-7). The z-axis (vertical) is translated in terms of toroidal laps. It is possible to notice how the trajectory loses its regularity due to the presence of a perturbative term.

4.2.1 Check of the energy convergence

The first study I performed is the relation between the average energy gained by the particles and the length of the simulation. It is reasonable to think that the average gained energy does not depend on the interaction time between the wave and the particle. Over long periods, the gains and the losses of energy balance themselves and the average energy converges to a final value. Only in low-periods simulation it is possible to have different value of energy because the system has not already reached the stability.

In figure 4.2.4, the average energy gained by the particles is plotted as a function of the length of the simulations. These times correspond to the complete duration of the simulation, so they also include the time needed from the $f(t)$ function to switch on/off the perturbation. This time is usually 1/5 of the total simulation length (section 2.2.2).
Every point in the graph is the average of 180 independent simulations of particles with initial energy lower than 100eV that interact with a single (1,-7) low-frequency wave, the one with lower frequency in the spectrogram.
It is possible to see the exact behaviour described previously. From 0 to $1000\tau_A$, the average energy decreases, but over than, the energy remains stable in time.
The error bars are simply computed by the mean squared displacement (msd) of the related set of simulations. The fact that the error bars' size reduces with the length of the simulations is due to the fact that longer simulations have a bigger number of data and the msd is proportional to the inverse of the number of points.

This gives robustness to our results, because it shows that the average energization does not depend on when the perturbation is switched-off in respect to the particle motion. It allowed us to set the total simulation length to the $1000\tau_A$, without including in the results errors due to the no reached energy convergence.
A possible way to improved this result is to repeat the same calculation varying the shape of $f(t)$. It may show that the average energization does not depend on how the perturbation is inserted in the system.

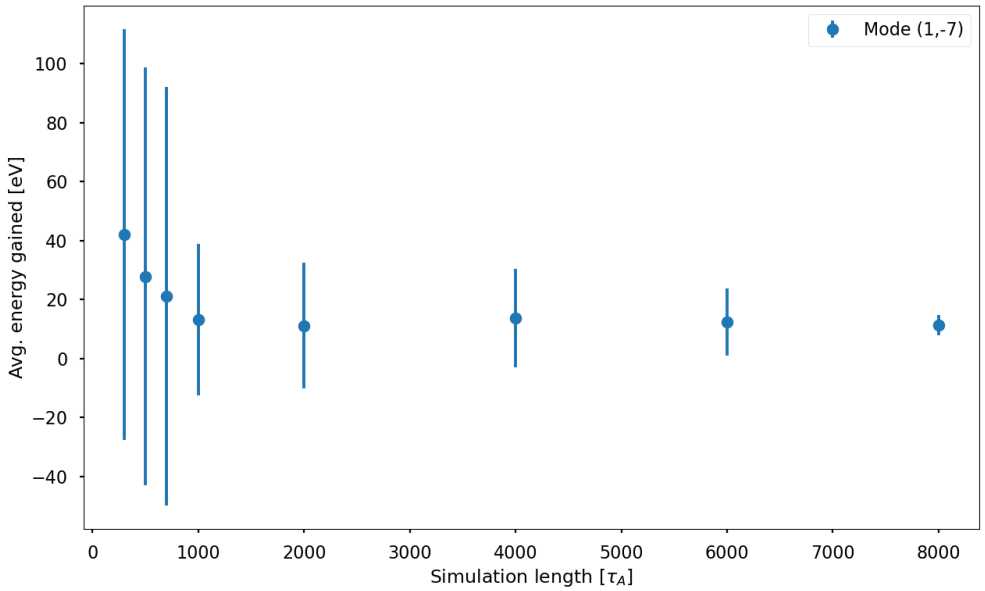

Figure 4.2.4: Average energy gained by the particles as a function on the simulation length. It is possible to see that the gain converges after the time of $1000\tau_A$. The error bars were computed by the mean squared displacement of the data. The big size of the errors bars of the faster simulations are due to the minor quantity of data.

4.2.2 Study of the heating as a function of the wave-amplitude

The ion energization should have a strong dependence on the wave amplitude: in our modelling the amplitude corresponds with the vector potential, so a higher amplitude corresponds to more energetic magnetic modes.
In order to study this relation, it has been decided to perform simulations varying the amplitude of the single waves. The simplest way to do this is to introduce an multiplicative factor α and to apply it to the definition of the j-esimal component of the perturbation field of equation 2.2.3:

$$A_j^{m,n}(r,\theta,z,t) = \alpha \cdot A_j^{m,n}(r) \cdot cos(\vec{k}\cdot\vec{r} - \omega t) f(t) \tag{4.2.1}$$

The multiplicative factor α was varied in a range of [0.5,12].
Another reason of the introducing the α is that we do not know actually the real amplitudes of the magnetic modes, we only have the results of the MHD modelling. With this amplitude scan, we want to show that the ion energization is always present if the perturbation is active ($\alpha > 0$).

Figure 4.2.5 shows the average energy gained by the particles as a function of the amplitude factor α, for two different waves: (1,-7) and (1,-8). For every α-value, 180 independent simulations have been performed. It was considered particles with initial energies lower than 100eV and initial positions between [0.1,0.4]r/a. The energy limit was chosen for two principal reasons: the first is that 100eV is the order of magnitude of the particle energy observed in the RFX-mod machine, and the second is that the integration of the equations of motion starts to diverge with too high energies. It was decided to start with particles in the inner part of the cylinder because the vector potential seems to be more regular in that region.

This figure shows two important results. The first one is that the average energy gain is positive for both magnetic modes and increases with the α value. This is the evidence that an ion energization is occurring in the simulations and it depends on the wave amplitude.

The orange curve, mode (1,-7), shows that the heating rapidly changes when the wave amplitude is increased from its magnitude. For $\alpha < 1$, the gained energy jumps near to the zero value very quickly. This is consistent with the ion-heating model, because when $\alpha = 0$, the system is only composed by the axisymmetric field and the particle cannot be heated. For $\alpha > 1$, the heating increases rapidly to tens of eV.
The blue curve, instead, increases with a very low rate: it can be also noticed a steps-like behaviour of the energy. It is reasonable to think that the two curves should show the same profile, but with different scales due to the big difference of amplitudes of the two modes, showed in figure 4.2.6.

The second result is that different waves with same amplitude can heat the particles by the same amount of energy. In figure 4.2.6, it is shown the ratio between the modules of amplitudes of the vector potential components of the two magnetic modes (left) and the ratio between the axisymmetric mode and the two perturbations (right).
The first shows that the magnetic mode (1,-7) is at least 5/6 times bigger than the other one. The second one shows that there is, almost everywhere, at least one order of magnitude of difference between equilibrium and perturbation fields. From the first image, we can assume that if the ratio of the two amplitude factors $\alpha^{1,-8}/\alpha^{1,-7}$ becomes of the order of 6, the amplitudes of the two waves can be considered equivalent.
So, the red dashed line in figure 4.2.5 shows that the blue points near to $\alpha = 12$ starts to have similar energy gain to the orange point at $\alpha = 2$. This is an interesting result that confirms that the wave amplitude is the most relevant parameter involved in the ion acceleration.

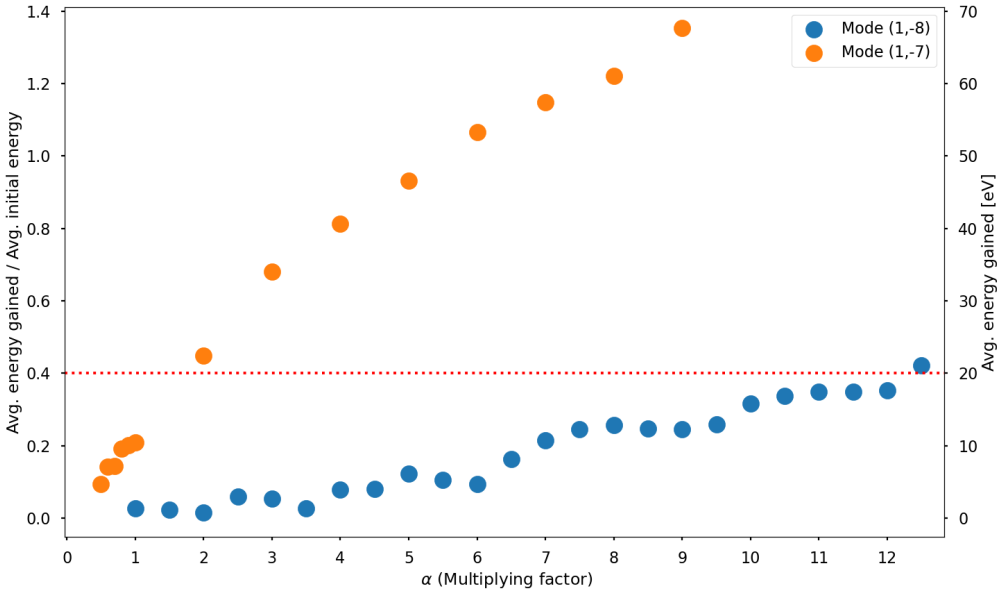

Figure 4.2.5: Average energy gain of the particles as a function of amplitude factor f. Every point is given by the average of 180 independent simulations. It is possible to see that the average heating is proportional to the wave amplitude, for both modes. The red dashed line shows that waves with same amplitude produce the same heating.

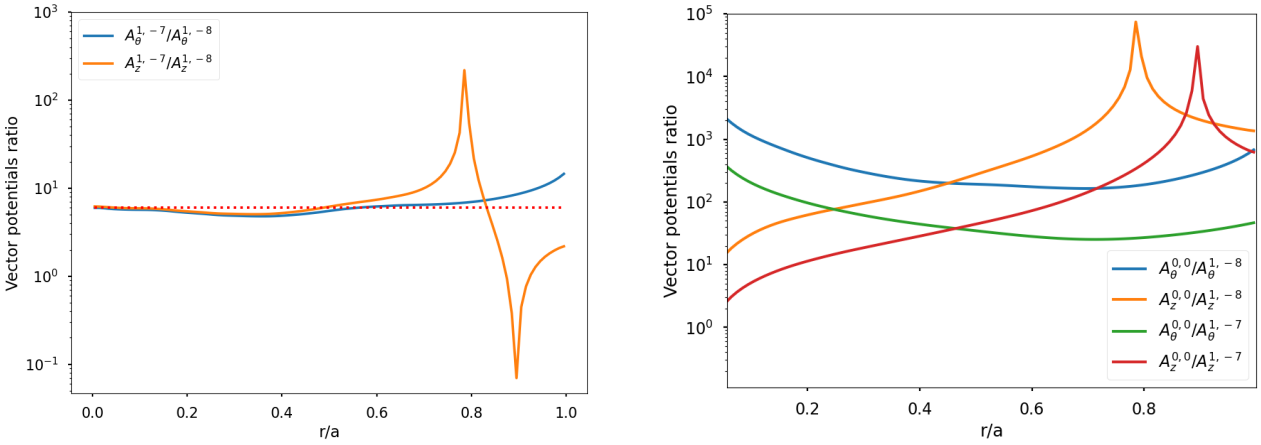

Figure 4.2.6: Left: Ratio between the absolute value of the vector potential components of the mode 1,-7 and the mode 1,-8. Right: ratio between the absolute value of the axisymmetric field vector potential and the two modes. The y-axis presents the log-scale due to the huge difference between equilibrium and perturbation fields.

4.2.3 Temporal evolution of energy distribution

An interesting result is given by the study of the temporal evolution of the energy distribution of a set of particles. It allows us to estimate the percentage of particles that are energized by the wave and to see if there are population of particles at precise energies.
The figure 4.2.7 shows 6 snapshots, one every $200\tau_A$, of the temporal evolution of the energy distribution of a set of 1000 independent simulation of cold ions. With the term cold we mean particles with initial energy lower than 1eV. This simulation was performed with a single wave, the first peak of the (1,-7) spectrum. The multiplying factor was set to $\alpha = 4$ in order to better observe the energy distribution.

The first image represents the initial configuration of the simulation, 1000 independent cold particles distributed at energy lower than 1eV. The small red figure on the right of each plot represents the perturbation vector potential as a function of the time. It is possible to see that, thanks to the shaping function $f(t)$, the wave starts at $200\tau_A$ and ends to $800\tau_A$. The vertical blue line represents the temporal instant of the snapshot.
The second plot corresponds to the time instant in which the perturbation reaches the maximum amplitude, i.e. when the $f(t)$ function becomes 1. It is possible to notice that as soon as the perturbation is introduced particles start to be heated. The third and the fourth plots show the behaviour of the energy during the interaction with the complete wave. By studying this phase more in detail, it is possible to see that the energy distribution changes continuously. In particular, it was possible to notice an oscillating behaviour: the energies seem to increase until values near 300eV and then they return to low energies. By observing the correspondent wave amplitude on the graphs, it seems that when the wave increases its amplitude the energies are increasing too, and viceversa.

The fifth figure of 4.4.7 corresponds to the instant at which the perturbation started to decrease due to the $f(t)$ function. At this time, two different populations of particles can be noticed, one at low energy ($E < 100eV$) and one at high energy ($E > 260eV$).
During the complete switching-off of the perturbation, reached in the sixth picture, the two populations merge creating an undefined final distribution.

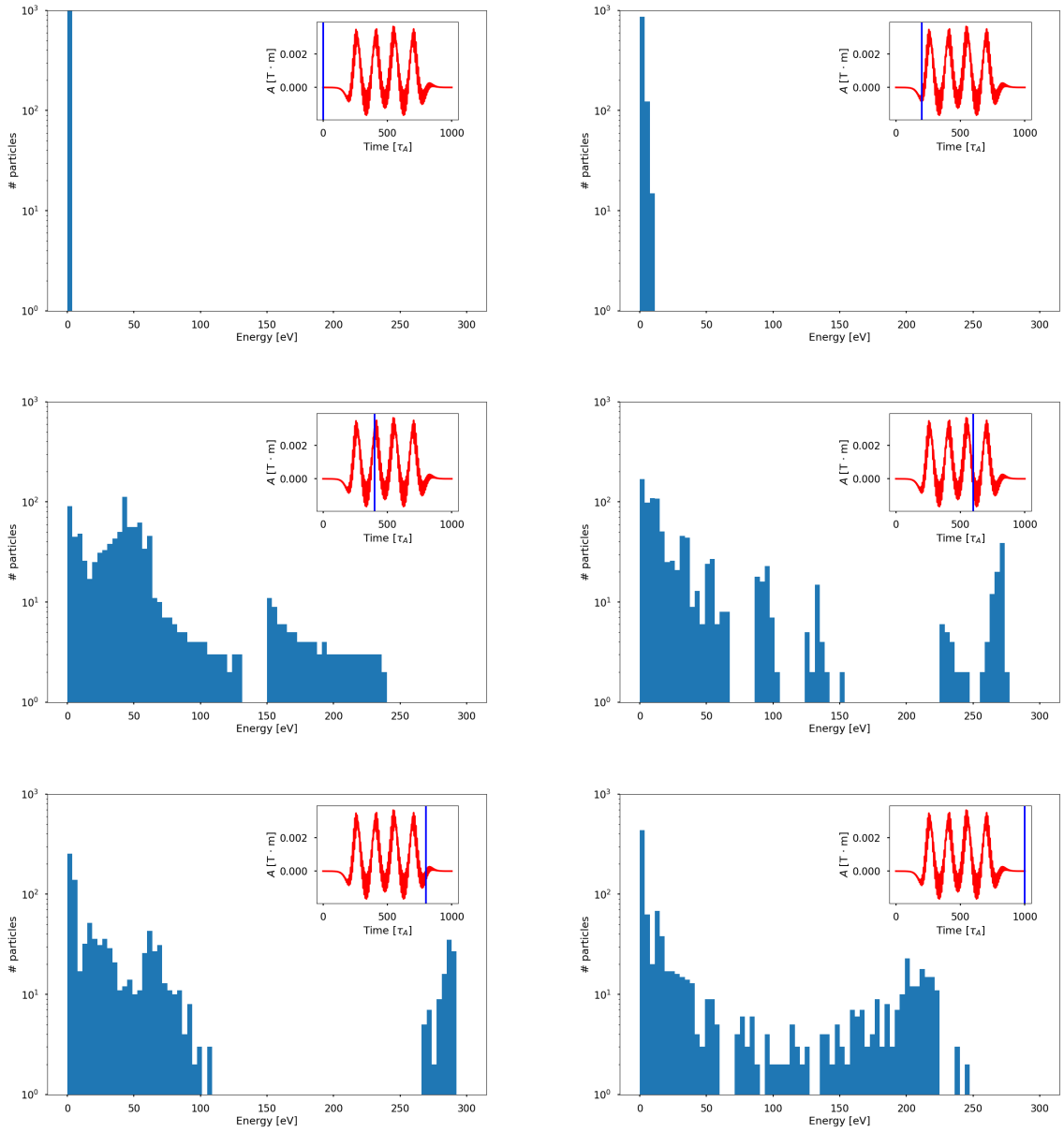

Figure 4.2.7: Temporal evolution (From left to right and from top to bottom) of the energy distribution of a set of 1000 cold particles. The red curve shows the amplitude of the perturbation and the vertical blue line the temporal instant of the snapshot. In the last figure, it is possible to see that there is population of particles that are heated by the wave.

The peak at low energy (6-th figure) contains almost the 50% of the initial particles, it means that the other 50% have been energized by the wave. The two biggest populations are between [0,50]eV and [150,230]eV. There is no evidence of particles heated at temperatures higher than 250eV.

It is possible to note that the final energy distribution is not the Maxwell-Boltzmann one, which is the one expected in an equilibrium plasma. The reason of this difference is the assumption of neglecting particle interactions. Without collisions, particles cannot thermalize inside the plasma, so they cannot reach the M-B distribution [11].

The same type of study was also applied to simulations with different temporal lengths. It was noticed that for the longer ones, the behaviour was the same. The oscillating central part became longer, but the final distribution was basically the same.
The shorter ones usually ended with a final distribution more spread in energy. It was more difficult the see the secondary population at high energy because they were more equally distributed along the x-axis.

4.3 Simulations with a set of Alfvénic turbulences

A further generalization of the heating modelling is given by the introduction of multiple different low-frequency waves that propagate inside the system. This generalization makes the system more similar to the real case, in which, during a magnetic reconnection event in a RFP plasma, a large spectrum of Alfvénic turbulences is generated and all of them interact with the particles. The ion heating is not a linear heating, so it is not sufficient to increase the number of the perturbations to expect a higher energization. In principle, the interference between the waves could annihilate the heating.

The modelling equations can be easily generalized to the presence of a N-number of waves by introducing in the vector potential, equation 2.2.22, other terms connected to different waves.
This generalization has two different applications that will be studied separately: the first one is to introduce in the system waves with different helicity and the second one is to combine several waves with same helicity (so extracted from the same spectrogram). The second case will be discussed in the next section.
In the real case, the complete spectrum of Alfvénic turbulence is a sum of the two described situations. The version of eq. 2.2.22 for the different helicity case is the following:

$$\vec{A}(r,\theta,z,t) = \vec{A}^{0,0}(r) + \alpha \sum_{m,n} \vec{A}^{m,n}(r) \cdot cos(\vec{k}^{m,n} \cdot \vec{r} - \omega^{m,n} t) f(t) \tag{4.3.1}$$

The first simple case is considering the presence of both the magnetic modes (1,-7) and (1,-8). The main reason of this calculation is the possibility to compare the results with the single-wave simulations, described previously in figure 4.2.5.
The equation 4.3.1 could be written as:

$$\begin{aligned} \vec{A}(r,\theta,z,t) = \vec{A}^{0,0}(r) + \alpha \cdot \vec{A}^{1,-7}(r) \cdot cos(k_r^{1,-7} r + \theta + \frac{7z}{R_0} - \omega^{1,-7} t) f(t) + \\ + \alpha \cdot \vec{A}^{1,-8}(r) \cdot cos(k_r^{1,-8} r + \theta + \frac{8z}{R_0} - \omega^{1,-8} t) f(t) \end{aligned} \tag{4.3.2}$$

It was decided to apply the same multiplying factor α for the two waves, in this way it was possible to maintain constant the ratio between the amplitudes.

In figure 4.3.1, there is a representation of the energy of the particles that interact with the combination of the modes (1,-7) and (1,-8) as a function of the time. On the left plot particles have same initial position, but different initial energy and, on the right, the contrary. Comparing this image with the 4.2.1, it is possible to note that the main difference is the change of amplitude of the oscillations during the interaction phase. In this case, the oscillations appear less regular both in amplitude and frequency, while in the previous case they could be approximated to a sinusoidal shape. This is clearly an effect of waves interference. Also in this case there is evidence of energization.

The blue points of figure 4.3.2 represents the average energy gained by particles interacting with the same combination of modes, as a function of α. Each point was obtained by the average of 180 independent simulations, with the same initial conditions described in section 4.2.2. Comparing this curve with the ones in figure 4.2.5 (the single-wave simulations), it is possible to notice a linear behaviour of the heating. The curve given by the combination of the two modes is comparable with the sum of the two single-wave curves.

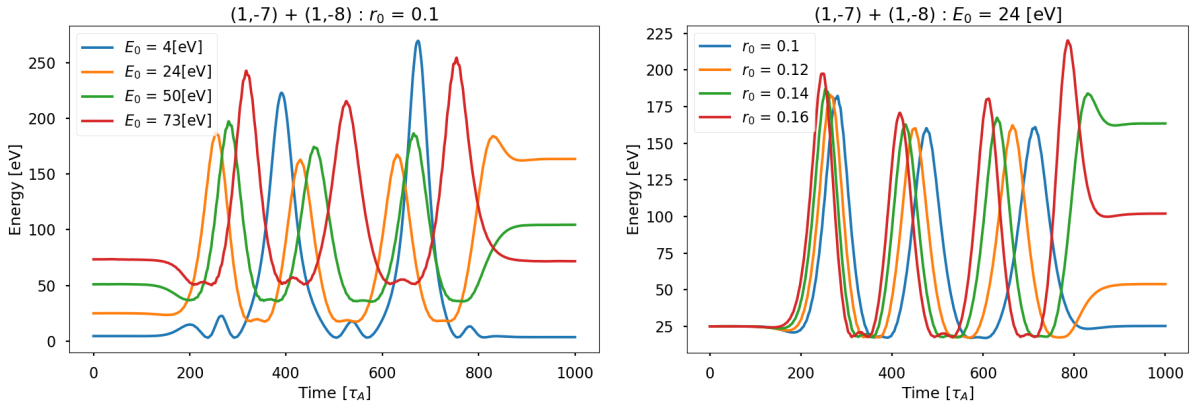

Figure 4.3.1: Temporal evolution of the energy for two different sets of simulations. At left, 5 particles with different initial energies, but with the same initial position. At right, viceversa, same energies but different positions.

4.3.1 Simulations of several waves with same helicity

As mentioned before, it is possible to generalize the eq. 2.2.22 in the case of N waves obtained from the same spectrogram, so with the same helicity. In the spectrograms of section 4.1, it is possible to see that each mode (m,n) has many low-frequency peaks with amplitudes comparable to the biggest one. For completeness, it was decided to observe the difference in energization between the cases of single wave and a set of these low-frequency peaks.
The equation 2.2.22, for the given mode (m,n) with N different waves taken from its spectrogram, can be written as follows:

$$\vec{A}(r,\theta,z,t) = \vec{A}^{0,0}(r) + \alpha \sum_{p=1}^{N} R_p \cdot \vec{A}^{m,n}(r) \cdot cos(\vec{k}^{m,n} \cdot \vec{r} - \omega^{m,n} t) f(t) \tag{4.3.3}$$

The R_p factor represents the ratio between the first peak amplitude and the one of the p-esimal peak; it is always lower than 1 ($R_p = 1$ in case of p=1). These factors were computed by using the amplitude values given by the spectrograms, such as in the figure 4.1.3.

This type of simulations has been performed for the two magnetic modes (1,-7) and (1,-8) in order to observe the difference with the single-wave interactions. In both cases, only the first 5 peaks of the spectrograms have been considered. There are two main reasons of this choice. The first is that we did not want to insert waves with too high frequency (the 5-th peak has a frequency of $\approx 2.9 \cdot 10^6 Hz$), and the second is that the amplitudes become very low (one order of magnitude lower than the first peaks, $R_p < 0.1$) and they are not relevant.

In figure 4.3.2, the orange and the green points represent the results of these simulations. It can be noticed than in both cases there is an increasing of the average heating in respect to the single-wave simulations. This effect is more visible for the orange curve. This is due to the

bigger amplitude of the mode (1,-7). In that case, the secondary peaks contribute more to the heating than the (1,-8) case. The fact that the orange curve shows a heating of 40eV for the value $\alpha = 0.5$ instead of going to zero means that 5 half-amplitude (1,-7) waves are sufficient to heat a particle, while this is not true for the (1,-8) mode.

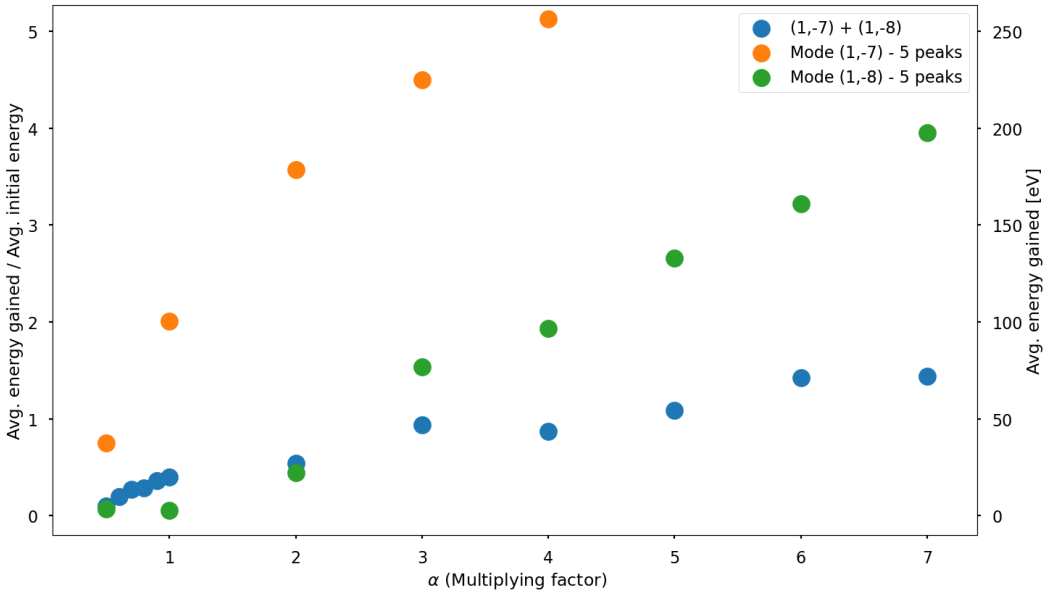

Figure 4.3.2: Average energy gain of the particles as a function of amplitude factor f. Every point is given by the average of 180 independent simulations. It is possible to see that the average heating is proportional to the wave amplitude, for both modes.

4.3.2 Simulations with sets of different helicity waves

The generalization of the modellling to a set of low-frequency waves is necessary in order to study more real systems. In a RFP plasma, there is a huge quantity of different waves that are generated during a magnetic reconnection event, as seen in the spectrogram analysis. These waves propagate inside the plasma a they can interact with the particles, heating them.
It is interesting to study the evidence of ion-heating due to the interaction with this huge set of different helicity waves.

The simulation code cannot sustain the presence of too many waves, because the integration algorithm starts to fail when the magnetic field becomes too chaotic. A reasonable compromise is the selection of a set of the most energetic modes of the system and the study of the particle interaction with the sum of these modes.
The easier way to select these magnetic modes is to observe their kinetic and magnetic energies. Figure 4.3.3 shows the average magnetic energy of the spectrum of all magnetic modes m=0 and m=1, computed by the SpeCyl code. Modes with m $>$ 1 were not considered because their energy was lower than the others.
The average is computed along the temporal window of the magnetic reconnection event and also along all the radial direction. The modes (1,-7) and (0,-1) are the most energetic ones. Around them, there are many other modes that are also important: from (1,-13) to (1,-7) for the m=1 and from (0,-6) to (0,-1) for m=0. These will be the two sets of magnetic modes from which the low-frequency waves will be extracted.

It was decided to test the energization for both the sets of waves separately, in order to observe the heating difference between the m=0 and the m=1 modes. For both cases, only the first peak of the spectrograms has been considered in order to not overload the simulation code. The vector potential equations of the two different sets are the following:

$$m = 1 \rightarrow \vec{A}(r,\theta,z,t) = \vec{A}^{0,0}(r) + \alpha \sum_{n=-13}^{-7} \vec{A}^{1,n}(r) \cdot cos(k_r^{1,n} r + \theta + \frac{nz}{R_0} - \omega^{1,n} t) f(t) \qquad (4.3.4)$$

$$m = 0 \rightarrow \vec{A}(r,\theta,z,t) = \vec{A}^{0,0}(r) + \alpha \sum_{n=-6}^{-1} \vec{A}^{0,n}(r) \cdot cos(k_r^{0,n} r + \frac{nz}{R_0} - \omega^{0,n} t) f(t) \qquad (4.3.5)$$

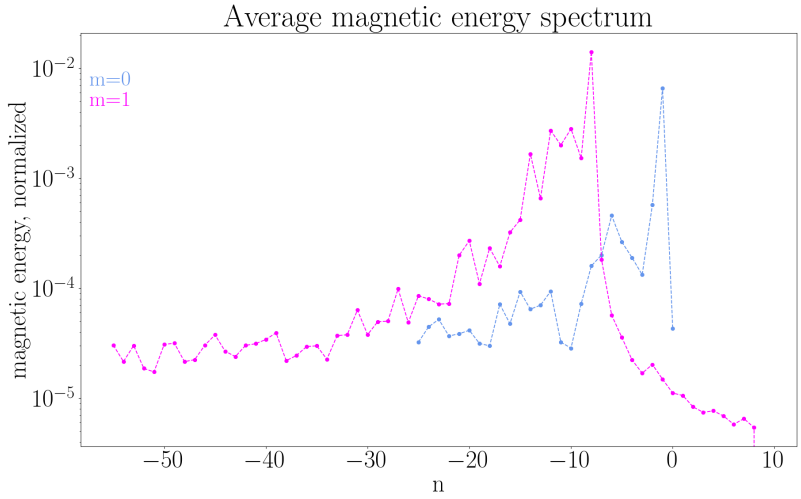

Figure 4.3.3: Average magnetic energy spectrum of all m=0 and m=1 modes. It is possible to notice that the most relevant modes are then ones (1,-13:-7) and (0,-6:-1).

As in the previous cases, sets of 180 simulations starting with energy lower than 100eV and initial position between [0.1;0.4]r/a have been performed for several multiplying factor α, and the average energy gained has been computed.
In figure 4.3.4, the average energy gained is plotted as a function of the α value. It is clear that there is a huge difference between the two sets of waves. The blue curve, which represents the $m = 1$ modes, increases rapidly with the α factor. At the level $\alpha = 1$, which is the case of not-modified waves, the average energy gained is of the order of 80eV. The set of m=0 modes, instead, is flat until the value $\alpha = 5$ in which the heating starts to be evident. The increasing behaviour is still very slow. This is probably due to the big difference in wave amplitudes between the two modes.
Another possible reason of this difference is that the magnetic modes with m=0 are more active in the outer region of the plasma and, in this simulations, the particles started their trajectory in the central region of the cylinder. Another set of simulations has been performed with particles starting near the surface of the cylinder, but not relevant heating difference was noticed.

In figure 4.3.5, an example of the trajectory of a test-particle which interacts with the set of m=1 modes is shown. If we compare this trajectory with the ones in figures 4.2.3, it is possible to see that motion is completely different. In this case, the trajectory is no more regular and it changes rapidly direction and rotation frequency. This is due to the chaotic field that is given by the mixture of different magnetic modes. The right picture of 4.3.5 shows the temporal evolution of

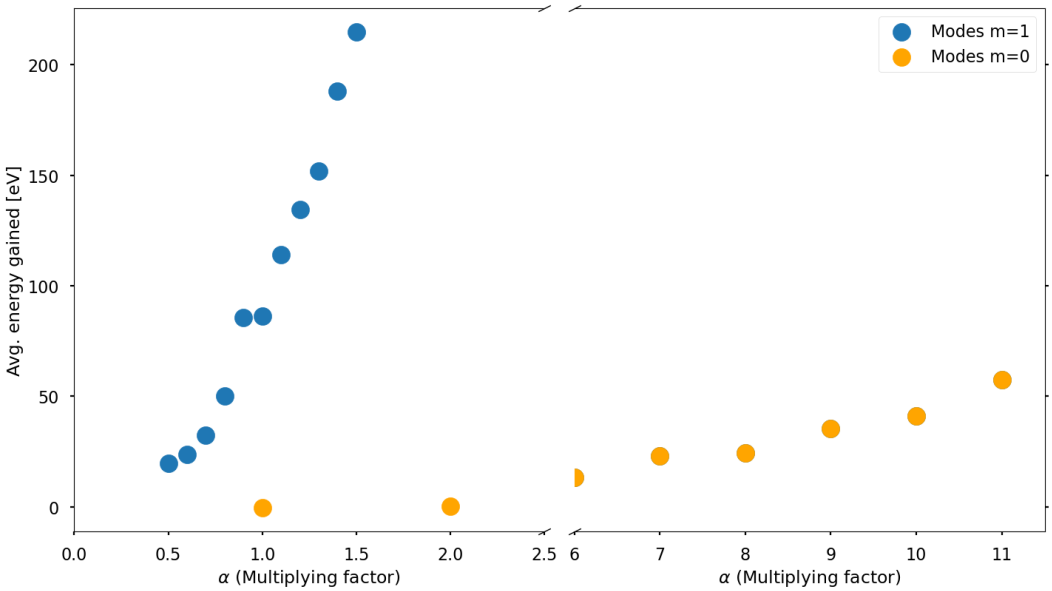

Figure 4.3.4: Average energy gain by the particles as a function of multiplying factor f. The two curves represent the sum of the main modes in a RFP plasma divided for different m values. Every point is given by the average over 180 independent simulations.

the energy of the particle along the same trajectory. It can be noticed that the particle increases its energy rapidly in the first part of the trajectory (blue zone) and in the rest of the simulation the energy oscillates around the average value of 100eV. This is another possible way to study the ion heating.

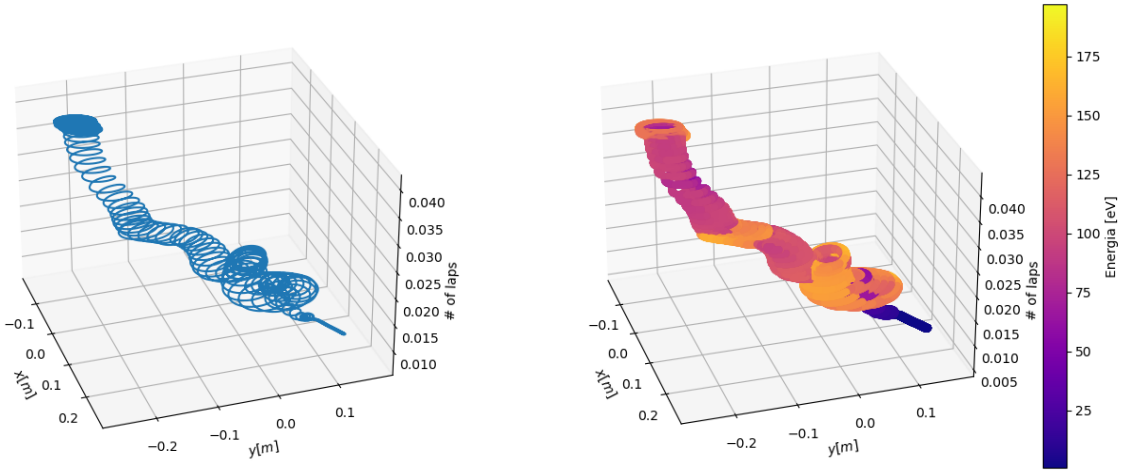

Figure 4.3.5: Trajectory of a test-particle that interacts with the set of the most energetic m=1 modes described in 4.3.2. On the right, temporal evolution of the energy of the test-particle (in the same trajectory) is described by the colorbar. Comparing with figure 4.2.3, it is possible to notice that the trajectory becomes complicated (and no more regular) as soon as the number of perturbations increases.

4.3.3 Study of the heating as a function of the test-particle mass

Another interesting result is given by the studying of the energization as a function of the mass of the test-particle.
In the paper [15], the mass-dependency of the ion-heating is studied in a RFP experiment during a magnetic reconnection event. It is shown that the heating seems to have a dependency on the particle mass, $\Delta E \propto m^{0.52}$. This result was obtained by studying 3 different plasmas (Hydrogen, Deuterium and Helium).

This is an interesting result because it is in contrast with the result obtained by the studying of the simple case of a particle that experiences the Lorentz force (eq 1.2.1). Given the equation of motion of the particle it is possible to obtain the velocity by integrating in time, as shown in eq. 4.3.6. If we substitute this expression of the velocity in the kinetic energy of the particle $E_k = \frac{1}{2}mv^2$, it is possible to see that $E_k \propto m^{-1}$.
So the temperature T, which is computed by averaging the E_k with a velocity distribution, is also proportional to the inverse of the mass.

$$m\frac{d\vec{v}}{dt} = q(\vec{E} + \vec{v} \times \vec{B}) \rightarrow \vec{v} = \frac{q}{m}\int(\vec{E} + \vec{v} \times \vec{B})dt \tag{4.3.6}$$

The difference between the two results is a signal of the presence of a physical phenomenum which is not fully understood.

In this section we want to try to replicate the results described in [15], considering the heating of different ions due to the interaction with a set of low-frequency waves.
In order to consider an equivalent case to [15], we have to impose a strong assumption on SpeCyl data. In fact, the SpeCyl simulation, which is used all along the thesis, has been performed considering a hydrogen plasma. This choice is connected to the plasma density that it is used to normalize the MHD equations (section 2.2.1).
We will assume that the same simulation can describe other types of plasmas, such deuterium and tritium ones, with the same perturbation spectra of the hydrogen one.
In order to have more significant results, it will be possible to perform new SpeCyl simulations with different plasma densities. This could not be done in this thesis due to time constraints.

Deuterium and a tritium have been chosen because they have the same electric charge of the hydrogen and their mass can be easily express as $m_D = 2m_H$ and $m_T = 3m_H$.
The change of the test-particle induces a cascade of changes in the normalizations described in the section 2.2.1 needed for the simulation code. In fact, the code integrates the Hamilton's equations of the eq. 2.2.18 considering the normalized mass $\tilde{m} = 1$. In order to maintain the same structure for the hamiltonian, the equation 2.2.9 must be changed, using the mass the j-th ion m_j instead of the hydrogen one. The same must be applied to the equation 2.2.10 if the new ion has a different electric charge. The cyclotron frequency of the ion must be also modified due to these changes.
In order to change the type of plasma, instead, we have to modify the normalization of the Alfvén time, eq. 2.2.4, which depends on the mass of the particles of the plasma. This will modify the frequencies of the waves extracted form the spectrograms and the duration of the fortran simulations.

It was decided to perform two different sets of simulations, one changing both test-particle and plasma and one changing only the test-particle (so using the original hydrogen plasma). The second case could be interesting for studying the energization of impurities present inside the plasma.

Sets of 180 simulations have been performed for each ion with the set of magnetic modes m=1, described in the section 4.3.2, with $\alpha = 1$.
In figure 4.3.6, the average energy gained by the 2 ions is plotted as a function of the ion mass, normalized to the hydrogen one.
The orange points correspond to the case of different test-particles in hydrogen plasma, while the blue ones are given by the assumption of different plasmas.
In both cases it is possible to see that the energization increases with the mass of the test-particle, but this increasing depends on the type of the plasma. The blue dashed line represents the function $g = E_H\sqrt{\frac{m_j}{m_H}}$ (E_H is the energy gained by the hydrogen) which is the behaviour obtained by experimental data [15].

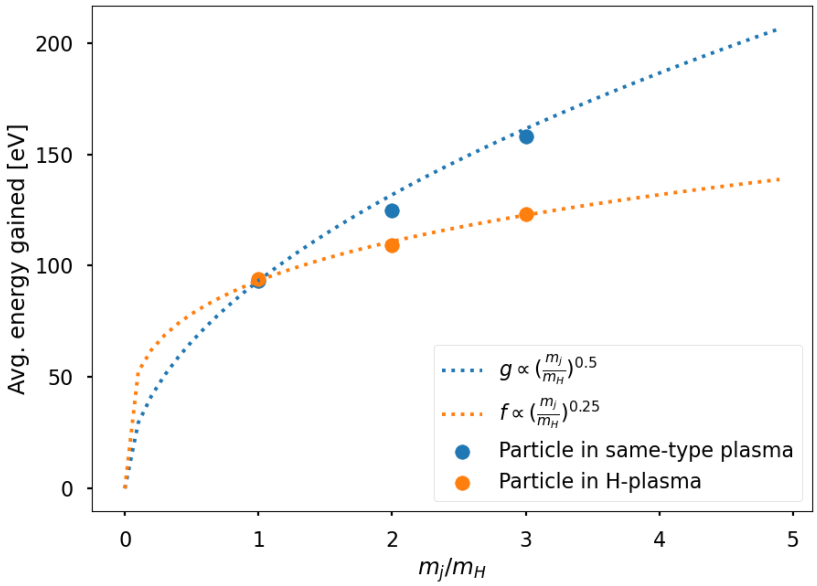

Figure 4.3.6: Average energy gained by three different ions (H,D,T) during the interaction with the set of the most energetic m=1 modes of SpeCyl simulation. The mass in normalized to the hydrogen mass. The dashed blue line shows the behaviour of a function $g \propto \sqrt{\frac{m_j}{m_H}}$, which is the one obtained in [15]. It is possible to see that the blue points are well described by this curve. The orange curve shows the behaviour of the orange points.

4.4 Heuristic interpretation of the ion heating

In [1], the ion heating by Alfvén waves was studied in order to try to explain the problem of the solar corona heating.
In that paper, a new picture for the ion heating mechanism was proposed. For measured waves amplitude, ion orbits were shown to cross quasi-periodically one or several separatrices in phase space. A separatrix is a trajectory in the phase space that has infinite period and divides different types of motions of a system. In figure 4.4.1, it is shown a simple case of a separatrix. It represents the phase space of the classical pendulum and it is possible to note that the red line, the separatrices, divide the phase space in the three different regions which correspond to different types of motion. Between the two red lines there is the classical oscillating motion of the pendulum, and out of them it starts to do clockwise or counter-clockwise rotations due to the high momentum.
The new mechanism sustains that each separatrix crossing cancels the adiabatic invariance and yields to a very strong energy transfer from the wave, and thus particle heating.

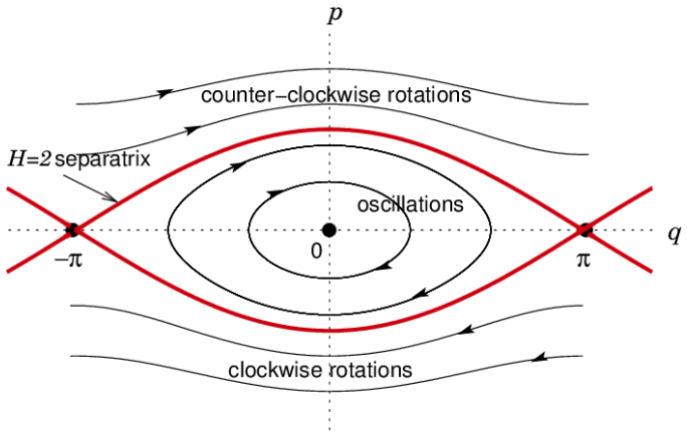

Figure 4.4.1: Example: the red line represents the two separatrices in the phase space of the classical pendulum system. They divide the phase space in three different regions.

This mechanism was studied in a simple 1D case, by the Hamiltonian description of the wave-particle interaction. The Hamiltonian was of the following shape:

$$H_1 = \frac{p^2}{2} + V(x) = \frac{p^2}{2} + \frac{x^2}{2} - Asin(x - \omega t + \phi) \tag{4.4.1}$$

This is two variable function (x, P_x) in which the potential term is the one of a harmonic oscillator modulated by a sinusoidal term.

In figure 4.4.2, three temporal instants of the 1D potential seen by the particle is shown (The figures are taken from [1]). It was possible to see that the system creates periodically a separatrix, whose shape changes periodically from a single-loop (central picture) to a double-loop one (right picture), until it disappears again.
It was seen that particle are accelerated by the crossing of these pulsating separatrices.

The hamiltonian of the 3D heating modelling presented in this thesis (eq. 2.2.17) is a function of 6 variables $(\vec{r}, \vec{P})$. The higher complexity does not allow to verify if the same heating mechanism is acting also in this case, in particular it is impossible to separate the kinetic part of the

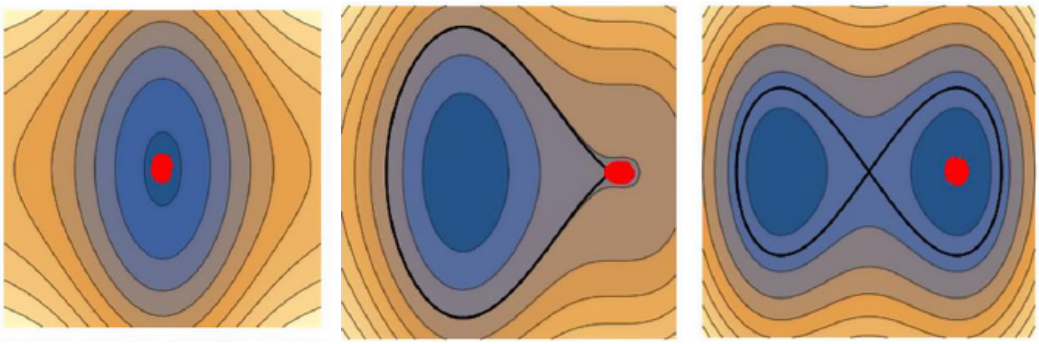

Figure 4.4.2: 3 temporal steps of a pulsating separatrix, black line. In the first image there is no separatrix. In the second it rounds a single-peak system and in the third ir rounds two peaks with a double-loop shape [1].

hamiltonian from the potential one. The 6D Hamiltonian can be written as following:

$$H(\vec{r},\vec{P}) = \frac{P_r^2}{2} + \frac{(P_\theta - rA_\theta)^2}{2r^2} + \frac{(P_z - A_z)^2}{2} \tag{4.4.2}$$

The only possible way to study the shape of a 6D Hamiltonian is to choice 2 of the possible variables and to observe 2D sections of the energy. This method does not guarantee to have a full description of the separatrix crossing, but it allows to have a partial vision of the system.
We have tried many different variable combinations and some interesting results have been obtained observing the phase-space along the x-y directions, near the center of the cylinder (r/a < 0.4).

The figure 4.4.3 shows the temporal evolution (in total $200\tau_A$) of the phase-space seen by the particle, which is represented by the red dot. This particles is interacting with a single (1,-7) wave, with $\alpha = 5$.
The snapshots must be read from left to right and from the top to the bottom. The color map goes from blue, which means low H, to white, which indicates a peak of the hamiltonian.
It is possible to notice that the structure of the Hamiltonian of the particle changes continuously in time. In the first row, the system shows a double-peak configuration in which the right peak is gradually vanishing.
The second row shows that for a small period of time ($\approx 50\tau_A$) the system remains with a single peak that seems to move from the left to the right part of the plot. In the third row, a secondary peak is gradually increasing the left part of the plots while the primary peak starts to vanish and, in the last row, the system slowly returns to the single peak configuration also present in the second row.

During all this process, the particle (red dot) is moving through these peaks following the trajectory described in figure 4.2.3. It is possible to notice that the figures of 4.4.3 have some similarities with the ones taken from the paper [1] (figure 4.4.2). The system seems to oscillate between single and double peak configurations: this could be a sign of the presence of a pulsating separatrix. This is only an heuristic conclusion, many other studies could be applied in order to better observe this mechanism, but in this thesis we limit presentation due to time problem.
An example of these studies could be to observe the temporal evolution of two 3D plots, one for the three spatial directions and one for the momenta, and comparing them with 2D sections as figure 4.4.3.
In this way, it maybe possible to observe a jump in the momenta space (so an increasing of energy) in correspondence of what we think could be a separatrix crossing.

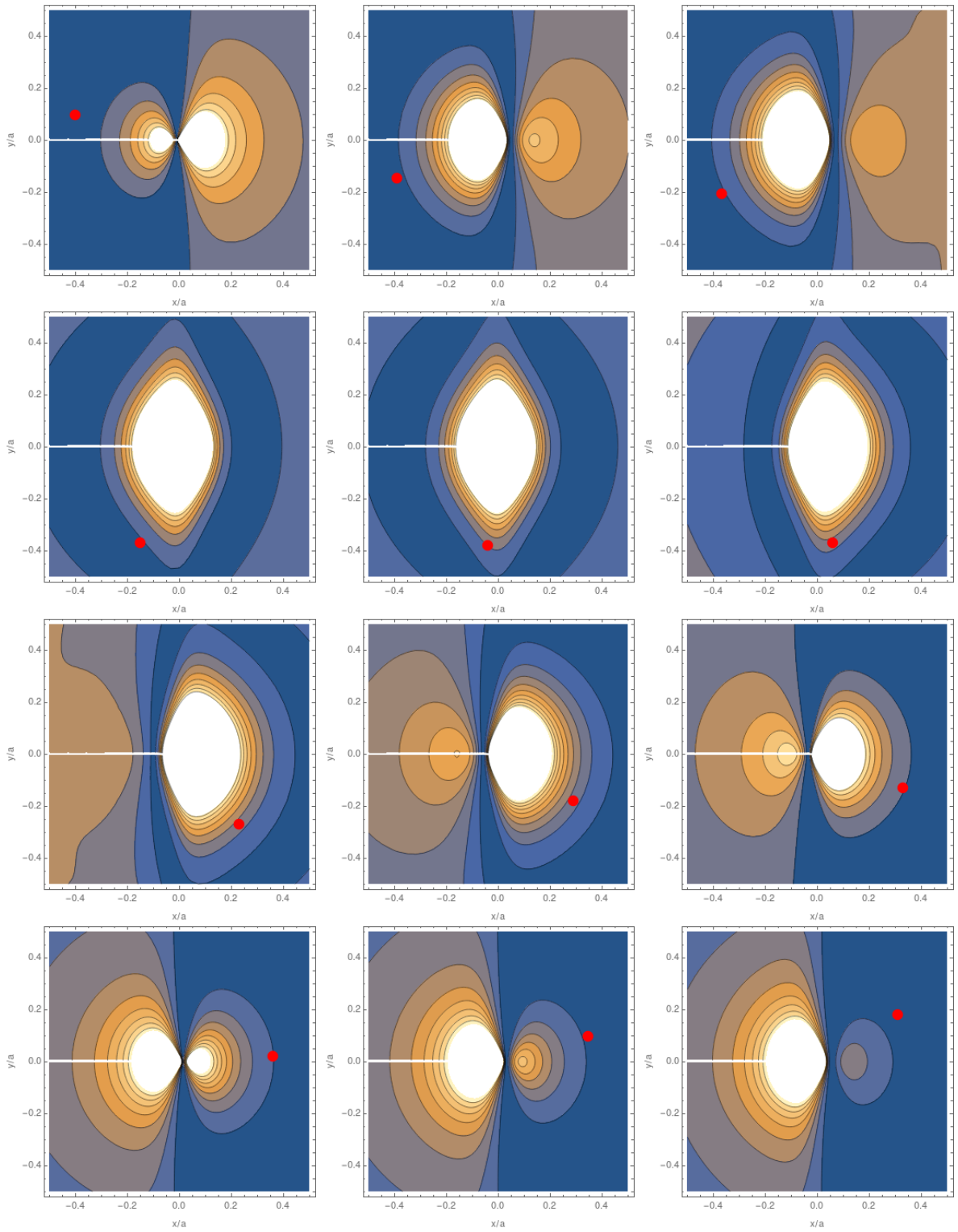

Figure 4.4.3: Temporal evolution (From left to right and from top to bottom) of the potential seen by the particles in the phase-space during a simulation. The red dot represents the particle. It is possible see a change of structure of the potential, which moves from a single maximum to a double maxima one and viceversa. This could be the sign of a pulsating separatrix.
The 12 snapshots represent a time of $200\tau_A$ of a simulation with a single wave of the mode (1,-7).

But, there is a big difference between the modelling presented in the paper and the one of this thesis: the paper shows that the energization happens only if the amplitude of the waves is higher than a precise threshold. The results obtained in this thesis show, instead, that the heating seems to have a smooth profile as a function of the multiplicative parameter α.
This is very interesting for the following reason: the heating is possible only if there is a mechanism that induces particle decorrelation, it must make the particles to forget which was their initial position and energy. In case of stochastic heating, the presence of many different waves is the heating factor.
In [1], it was shown that the decorrelation is possible also with a single wave, but it is necessary that its amplitude is comparable with the equilibrium field (which is the threshold).
In this thesis, it is shown that the heating depends on the amplitude, but there is no a threshold. So, the mechanism that induced energization in this thesis is still unknown.

Chapter 5

Conclusions

The work presented in this thesis deals with ion heating by Alfvén waves produced in a magnetic reconnection event. The goal stated at the beginning was to observe if particles can be heated by the interaction with a set of low-frequency electromagnetic waves.
The work has been done by using a test-particle approach and the Hamiltonian description of the wave-particle interaction. The Alfvèn waves have been obtained from a magnetic reconnection event of a RFP plasma simulated with a 3D non-linear MHD code.
The heating has been studied for different combinations of Alfvénic perturbations, starting from the simplest case of a single wave and concluding with the set of the most energetic magnetic modes active during the reconnection event.
Hundreds of simulations have been performed varying many different parameters, such as the simulation length, the mass of the test-particle and the amplitudes of the perturbations. A statistical analysis of the energy distribution was also performed.
The most significant results obtained are summarized in the following points:

- By studying the energy temporal evolution of a test-particle which interacts with an Alfvénic turbulence computed by a 3D non-linear MHD modelling of a RFP plasma, it is possible to see an average increasing of the energy due to the wave interaction. This is proportional to the number of the perturbations active in the system and their amplitudes. The obtained results are comparable with the experimental ones of the major RFP experiments;

- The average energy gained by the test-particles has been studied as a function of the simulation length. It is observed that ion heating is independent on the interaction time with the Alfvén waves. The convergence of the energy is important for the reliability of the results;

- From a statistical analysis of the energy distribution of a set of 1000 independent simulations with a single perturbation, it is observed that at least the 50% of the test-particles are heated by the wave interaction;

- The ion heating has been studied as a function of the mass of the test-particle. By studying different test-particles in a hydrogen plasma, it is possible to see that the heating increases with the mass of the ion. A similar bahaviour is observed with the strong assumption of considering different type plasmas with the same Alfvénic turbulence computed by the SpeCyl code for the hydrogen case.

Despite the interesting results obtained, this thesis is only a starting point of research. There are many ways in which these results could be implemented and improved, and also many other systems that could be explored.
In the following points we will present a list of some of the possible improvements that could be applied and some future applications:

- One of the problems encountered in this thesis is the failure of the symplectic integrator of computing the particle trajectory for a too widespread number of Alfvénic perturbations. It would be possible to introduce a new integrator in order to observe the heating of the combination of all the magnetic modes computed by SpeCyl, which is nearer to the real case;

- By performing new SpeCyl simulations for different types of plasmas, it would be possible to obtain a more significant results to be compared with the experimental results of [15]. Due to the length of the simulations involved, it was not possible to do it during the thesis period;

- Another interesting result could be given by the changing of the shaping function $f(t)$. Introducing new functions with different temporal profiles may be show different heating properties. It would be also interesting to introduce $f(t)$ function comparable to the real crashing profile of the fields during a reconnection event;

- An interesting future application could be the studying of different plasmas configurations, such as tokamak devices. It would be interesting to compare the ion heating with different types of Alfvénic turbulences.

Appendix A

Appendices

A.1 Liouville's theorem

Liouville's theorem is one of the most important theorems of statistical mechanics. Lets consider the trajectory in the phase-space of a single component of an ensemble. We define $\rho_e(q_s, p_s, t)$ the density of particles of that ensemble.
The theorem states that the time derivative of this density as we move along the selected trajectory is zero:

$$\frac{D\rho_e}{Dt} = 0 \tag{A.1.1}$$

If (q_s,p_s) and ($q_s + \delta q_s$, $p_s + \delta p_s$) are two successive states of the system at time t and $t + \delta t$ then:

$$\frac{D\rho_e}{Dt} = \lim_{\delta t \to 0} \frac{\rho_e(q_s + \delta q_s, p_s + \delta p_s, t + \delta t) - \rho_e(q_s, p_s, t)}{\delta t} \tag{A.1.2}$$

Making a Taylor expansion of the term $\rho_e(q_s + \delta q_s, p_s + \delta p_s, t + \delta t$ and substituting it into this equation we have:

$$\frac{D\rho_e}{Dt} = \frac{\partial \rho_e}{\partial t} + \sum_s \dot{q}_s \frac{\partial \rho_e}{\partial q_s} + \sum_s \dot{p}_s \frac{\partial \rho_e}{\partial p_s} \tag{A.1.3}$$

The next step is to show that the right side of this equation in equal to zero. This can be done by deriving the equation of continuity of mass.
Given ρ the density of the system, the mass will be the integral of the density over a volume V. The mass can change only due to a mass flux across the surface bunding that volume

$$\frac{\partial}{\partial t} \int \rho dV = - \int \rho v \cdot ds \tag{A.1.4}$$

By applying the Gauss' theorem, the equation of continuity follows:

$$\frac{\partial \rho}{\partial t} + \nabla \cdot (\rho v) = 0 \tag{A.1.5}$$

If now we introduce in this equation the ρ_e and $v = (\dot{q}_s, \dot{p}_s)$ defined in the first part and we use the Hamilton's equations, it can be shown that:

$$\frac{\partial \rho_e}{\partial t} + \sum_s \dot{q}_s \frac{\partial \rho_e}{\partial q_s} + \sum_s \dot{p}_s \frac{\partial \rho_e}{\partial p_s} + \rho_e \sum_s \left(\frac{\partial \dot{q}_s}{\partial q_s} + \frac{\partial \dot{p}_s}{\partial p_s} \right) = 0 \tag{A.1.6}$$

An important corollary of this theorem is the following. Suppose that there are n ensemble points inside the initial phase-space volume $d^n q_s d^n p_s$ and after some time it becomes $d^n q'_s d^n p'_s$. If the two densities are ρ_e and ρ'_e, it follows that:

$$\rho_e d^n q_s d^n p_s = \rho'_e d^n q'_s d^n p'_s \tag{A.1.7}$$

Since the Liouville theorem implies that the density cannot change in time, it follows that $d^n q_s d^n p_s = d^n q'_s d^n p'_s$ which means that the volume in tha phase-space cannot change.

A.2 Coordinates and Fourier transform

The cylindrical coordinates (r,θ,z) are defined as the polar coordinates in the x-y plane, with the z which represents the distance from that plane. In simple scheme is shown in figure A.1.
The simplest way to work with a toroidal geometry is to extend the cylindrical coordinates with a precise boundary condition. In fact, the torus is nothing but a cylinder that is closed to itself along the z-direction.
The trick is to define the z coordinate as follows: z = $R_0\phi$, where R_0 is the major radius of the torus. In this way, a periodic boundary condition is set along the z direction: it is possible to substitute the z coordinate with another angular coordinate ϕ. Given R_0, every time that we make a lap around the torus, we are moving of $z = 2\pi R_0$ which corresponds to a complete circle of $\phi = 2\pi$:

$$\phi = 2\pi \left[\frac{z}{2\pi R_0}\right] = \frac{z}{R_0} \tag{A.2.1}$$

So, the toroidal coordinates can be defined as (r,θ,ϕ). In figure A.2.1, there is a schematic representation of the toroidal coordinates.

Another possible way to work with toroidal geometry is to use a Fourier expansion over the angular directions. For example, a generic field A can be written as:

$$A(r,\theta,\phi) = \sum_{m,n} A_{mn}(r) e^{i(m\theta + n\phi)}, \tag{A.2.2}$$

where m,n are a pair of integer indices and $A_{mn}(r)$ is the Fourier component of the mode (m,n). In this case, the component $A_{(0,0)}$ is the axisymmetric part of the field.
This type of reference is helpful to describe field perturbations.

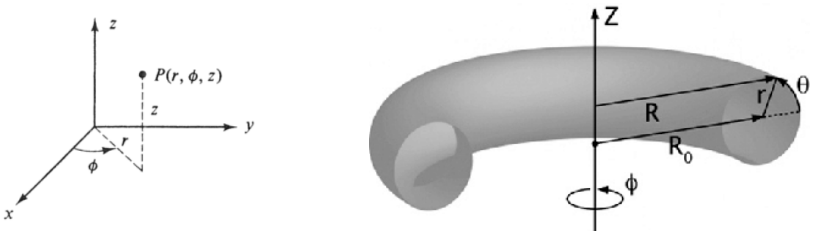

Figure A.2.1: Schemes of cylindrical coordinates (left) and toroidal coordinates (right).

A.3 Wave vector in cylindrical coordinates

The differential arc-length along a coordinate curve u^i, which I denote by dl(i) is [1],

$$dl(i) = |dR(i)| = \sqrt{dR(i)R(i)} \tag{A.3.1}$$

and

$$dR(i) = \frac{dR}{\partial u^i} du^i = e_i du^i = \sqrt{g_{ii}} du^i \hat{e^i} \tag{A.3.2}$$

implying that:

$$dl(i) = \sqrt{g_{ii}} du^i \tag{A.3.3}$$

In cylindrical geometry this means that $dl = dr\hat{r} + rd\theta\hat{\theta} + dz\hat{z}$. From these considerations, the computation of the angular component of the wave vector is very simple. For example, to compute k_θ we have to divide 2π for the integration of r$d\theta$ along one cycle in the poloidal direction. This quantity coincide with $r(2\pi/m)$. The analogous can be done for the z component.

A.4 Products of variables in Fourier space

Given two variable B_i and v_j defined as the equation X, with mode numbers respectively (m,n) and (m',n'), their product can be performed in the following way:

$$v_j B_i = \sum_{m',n'} \sum_{m,n} v_j^{m',n'} e^{i(m'\theta+n'\phi)} B_i^{m,n} e^{i(m\theta+n\phi)} \tag{A.4.1}$$

$$v_j B_i = \sum_{m',n'} \sum_{m,n} v_j^{m',n'} B_i^{m,n} e^{i(m+m')\theta} e^{i(n+n')\phi} \tag{A.4.2}$$

Using a property of the delta function, it is possible to simplify the notation introducing new mode numbers $\tilde{m}$ and $\tilde{n}$, that are defined as $\tilde{m} = m + m'$ and $\tilde{n} = n + n'$:

$$e^{i(m+m')\theta} = \sum_{\tilde{m}} e^{i\tilde{m}\theta} \delta_{\tilde{m},m+m'} \qquad e^{i(n+n')\phi} = \sum_{\tilde{n}} e^{i\tilde{n}\phi} \delta_{\tilde{n},n+n'} \tag{A.4.3}$$

Applying this property to the 8.6 equation it follows that:

$$v_j B_i = \sum_{m',n'} \sum_{m,n} v_j^{m',n'} B_i^{m,n} \sum_{\tilde{m}} e^{i\tilde{m}\theta} \delta_{\tilde{m},m+m'} \sum_{\tilde{n}} e^{i\tilde{n}\phi} \delta_{\tilde{n},n+n'} \tag{A.4.4}$$

$$v_j B_i = \sum_{\tilde{m}} \sum_{\tilde{n}} e^{i\tilde{m}\theta} e^{i\tilde{n}\phi} \sum_{m,n} \sum_{\tilde{m}-m,\tilde{n}-n} B_i^{m,n} v_j^{\tilde{m}-m,\tilde{n}-n} \tag{A.4.5}$$

Equation 8.9 follows from the application of the Kronecker delta after the consideration that $\delta_{\tilde{m},m+m'} = \delta_{\tilde{m}-m,m'}$. The same holds also for the $\tilde{n}$ case.
At this point it is possible to re-write the equation,

$$v_j B_i = \sum_{\tilde{m},\tilde{n}} \left(\sum_{m,n} B_i^{m,n} v_j^{\tilde{m}-m,\tilde{n}-n} \right) e^{i(\tilde{m}\theta+\tilde{n}\phi)} \tag{A.4.6}$$

which is the one presented in the equation x. I follows that:

$$(v_j B_i)_{\tilde{m},\tilde{n}} = \sum_{m,n} B_i^{m,n} v_j^{\tilde{m}-m,\tilde{n}-n} \tag{A.4.7}$$

A.5 Symplectic integrators

The symplectic integration of Hamiltonian dynamical systems is by now an established technique. Standard integrators do not generally preserve the Poincaré integral invariants of a Hamiltonian flow and cannot hope to capture the long-time dynamics of the system.
Typically their numerical diffusion causes orbits to be attraced to elliptic orbits, or, creates completely unphysical attractors.The non-conservation of integral invariants presumably corrupts the long-time statistics of the flow.

Symplectic integrators are a numerical integration scheme for Hamiltonian systems. They are designed for the numerical solution of Hamilton's equations:

$$\dot{p} = -\frac{\partial H}{\partial p} \qquad \dot{q} = \frac{\partial H}{\partial q} \tag{A.5.1}$$

The time evolution of these equations is a symplecto-morphism, meaning that it conserves the symplectic 2-form $dp \times dq$. A numerical scheme is a symplectic integrator if it also conserves this 2-form. Symplectic integrators also might possess, as conserved quantity, a Hamiltonian which is slightly perturbed from the original one. By virtue of these advantages, the SI scheme

has been applied to the calculations of long-term evolution of chaotic Hamiltonian systems.

A widely used class of symplectic integrator is formed by the splitting methods. Assume that the Hamiltonian is separable:

$$H(q,p) = T(p) + V(q) \tag{A.5.2}$$

The set of Hamiltonian's equations given by this equation can be expressed as:

$$\dot{z} = z, H(z) \tag{A.5.3}$$

in which z=(q,p) denotes the canonical coordinates and , is a Poisson bracket. Given $D_H = \cdot, H$ an operator that returns the Poisson bracket, the previous equation can be written as:

$$\dot{z} = D_H z \rightarrow z(\tau) = e^{\tau D_H} z(0) \tag{A.5.4}$$

The symplectic integrators scheme approximates the time-evolution operator $e^{\tau(D_H)}$ by the product of operators as:

$$e^{\tau(D_H)} = e^{\tau(D_T + D_V)} = \prod_{i=1}^{k} e^{c_i \tau D_T} e^{d_i \tau D_V} + O(\tau k + 1) \tag{A.5.5}$$

where c_i and d_i are real numbers, k is an integer, the order of the integrator, and $\sum_i^k c_i = \sum_i^k d_i = 1$.

Each operator provides a symplectic map, so their product is also a symplectic map. Since $D_T^2 z = \{\{z, T\}, T\} = \{(\dot{q}, 0), T\} = (0, 0)$, we can conclude $D_T^2 = 0$. So, by using a taylor series to the exponentials:

$$e^{aD_T} = \sum_{n=0} \frac{(aD_T)^2}{n!} \tag{A.5.6}$$

with a real number. Combining the two previous equations and extending the concept to D_V, we get:

$$\begin{aligned} e^{aD_T} &= 1 + aD_T \\ e^{aD_V} &= 1 + aD_V \end{aligned} \tag{A.5.7}$$

In concrete,

$$\begin{bmatrix} q \\ p \end{bmatrix} \rightarrow \begin{bmatrix} q + \tau c_i \frac{\partial T}{\partial p}(p) \\ p \end{bmatrix} \tag{A.5.8}$$

$$\begin{bmatrix} q \\ p \end{bmatrix} \rightarrow \begin{bmatrix} q \\ p - \tau d_i \frac{\partial V}{\partial q}(q) \end{bmatrix} \tag{A.5.9}$$

Note that both of these maps are practically computable.

Bibliography

[1] Escande, D.F., Gondret, V. Sattin, F. *Relevant heating of the quiet solar corona by Alfvén waves: a result of adiabaticity breakdown.* Sci Rep 9, 14274 (2019).

[2] Bicák, J., Ledvinka, T. *General Relativity, Cosmology and Astrophysics* Springer (2004).

[3] Wesson, J. *Tokamaks* Clarendon press - Oxford, Third edition (2004).

[4] Stella, A., Guarnieri, M. et all. *The RFX magnet system.* Plasma physics and controlled fusion, 52, 095011 (1995).

[5] Kharkongor, D., Mahato, M.C. *Resonance oscillation of a damped driven simple pendulum.* Eur. J. Phys. 39 , 065002 (2018).

[6] Tsuturani, Bruce T., Lakhina, Gurbax S. *Some basic concepts of wave-particle interactions in collisionless plasmas.* Rew. of Geophysics,35, 97RG02200 (1997).

[7] Spagnolo, S., Zuin, M. et all. *Alfvén eigenmodes in the RFX-mod reversed-field pinch plasma.* Nucl. Fusion, 51, 083038 (2011).

[8] Soffer, A., Weinstein *Nonautonomous Hamiltonians.* J. Statistical Phy., vol. 93, nos 1/2, (1998).

[9] McLachlan, R.I., Atela, P. *The accuracy of symplectic integrators.* IOP Science, Nonlinearity 5 (1992)

[10] Finn, J.M., Chacòn, L. *Volume preserving integrators for solenoidal fields on grid.* Phys.of Plasmas 12, 054503(2005).

[11] Choudouri, A.R. *The physics of fluids and plasmas. An introduction for astrophysicists.* Cambridge Univerisity Press (1998).

[12] Nishikawa, K., Wakatani, M. *Plasma Physics.* Springer, third edition (2000).

[13] Bonfiglio, D., Chachòn, L., Cappello, S. *Nonlinear three-dimensional verification of the SPECYL and PIXIE3D magnetohydrodynamics codes for fusion plasmas* Phys. Plasmas 17, 082501 (2010).

[14] Kryzhanovskyy, A., Bonfiglio, D., et all. *Alfvén waves in reversed-field pinch and tokamak ohmic plasmas: nonlinear 3D MHD modeling and comparison with RFX-mod.* Nucl. Fusion 62, 086019, (2022).

[15] Fiksel G., Almagri, A.F., et all *Mass-dependent ion heating during magnetic reconnection in laboratory plasma.* PhysRevLett. 103, 145002 (2009).

[16] Cappello, S., Biskamp, D. *Reconnection processes and scaling laws in reverse field pinch magnetohydrodynamics.* Nucl. Fusion vol. 36, N. 5 (1996).

[17] Kusano, K., Tamano, T., Sato, T. *MHD simulation of the toroidal phase locking mechanism in a reversed field pinch plasma..* Nucl. Fusion vol. 31, N. 10 (1991).